USGS
science for a changing world

Prepared for the National Aeronautics and Space Administration

Geologic Map of the Taussig Quadrangle (V–39), Venus

By Antony W. Brian, Ellen R. Stofan, and John E. Guest

Pamphlet to accompany
Scientific Investigations Map 2813

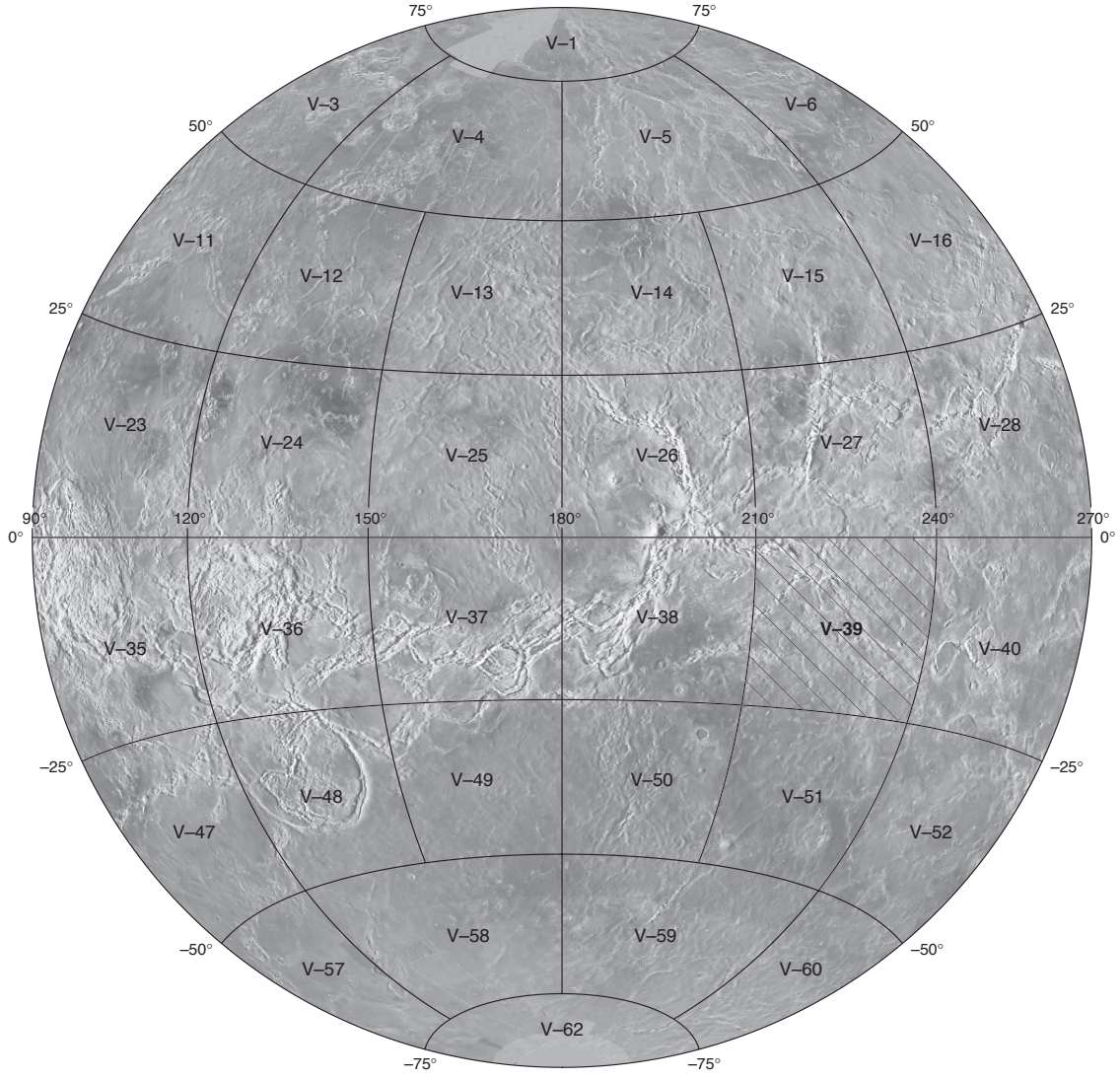

2005

U.S. Department of the Interior
U.S. Geological Survey

THE MAGELLAN MISSION

The Magellan spacecraft orbited Venus from August 10, 1990, until it plunged into the Venusian atmosphere on October 12, 1994. Magellan Mission objectives included (1) improving the knowledge of the geological processes, surface properties, and geologic history of Venus by analysis of surface radar characteristics, topography, and morphology and (2) improving the knowledge of the geophysics of Venus by analysis of Venusian gravity.

The Magellan spacecraft carried a 12.6-cm radar system to map the surface of Venus. The transmitter and receiver systems were used to collect three data sets: (1) synthetic aperture radar (SAR) images of the surface, (2) passive microwave thermal emission observations, and (3) measurements of the backscattered power at small angles of incidence, which were processed to yield altimetric data. Radar imaging and altimetric and radiometric mapping of the Venusian surface was accomplished in mission cycles 1, 2, and 3 from September 1990 until September 1992. Ninety-eight percent of the surface was mapped with radar resolution on the order of 120 m. The SAR observations were projected to a 75-m nominal horizontal resolution, and these full-resolution data compose the image base used in geologic mapping. The primary polarization mode was horizontal-transmit, horizontal-receive (HH), but additional data for selected areas were collected for the vertical polarization sense. Incidence angles varied between about 20° and 45°.

High-resolution Doppler tracking of the spacecraft took place from September 1992 through October 1994 (mission cycles 4, 5, 6). Some 950 orbits of high-resolution gravity observations were obtained between September 1992 and May 1993 while Magellan was in an elliptical orbit with a periapsis near 175 km and an apoapsis near 8,000 km. An additional 1,500 orbits were obtained following orbit-circularization in mid-1993. These data exist as a 75° by 75° harmonic field.

MAGELLAN RADAR DATA

Radar backscatter power is determined by (1) the morphology of the surface at a broad range of scales and (2) the intrinsic reflectivity, or dielectric constant, of the material. Topography at scales of several meters and larger can produce quasi-specular echoes, with the strength of the return greatest when the local surface is perpendicular to the incident beam. This type of scattering is most important at very small angles of incidence, since natural surfaces generally have few large tilted facets at high angles. The exception is in areas of steep slopes, such as ridges or rift zones, where favorably tilted terrain can produce very bright signatures in the radar image. For most other areas, diffuse echoes from roughness at scales comparable to the radar wavelength are responsible for variations in the SAR return. In either case, the echo strength is also modulated by the reflectivity of the surface material. The density of the upper few wavelengths of the surface can have a significant effect. Low-density layers such as crater ejecta or volcanic ash can absorb the incident energy and produce a lower observed echo. On Venus, there also exists a rapid increase in reflectivity at a certain critical elevation, above which high-dielectric minerals or coatings are thought to be present. This leads to very bright SAR echoes from virtually all areas above that critical elevation.

The measurements of passive thermal emission from Venus, though of much lower spatial resolution than the SAR data, are more sensitive to changes in the dielectric constant of the surface than to roughness. As such, they can be used to augment studies of the surface and to discriminate between roughness and reflectivity effects. Observations of the near-nadir backscatter power, collected using a separate smaller antenna on the spacecraft, were modeled using the Hagfors expression for echoes from gently undulating surfaces to yield estimates of planetary radius, Fresnel reflectivity, and root-mean-square (rms) slope. The topographic data produced by this technique have horizontal footprint sizes of about 10 km near periapsis and a vertical resolution on the order of 100 m. The Fresnel reflectivity data provide a comparison to the emissivity maps, and the rms slope parameter is an indicator of the surface tilts, which contribute to the quasi-specular scattering component.

TAUSSIG QUADRANGLE

INTRODUCTION

The Taussig quadrangle (V–39) of Venus extends from lat 0° to 25° S. and long 210° to 240° E. The area is named after the 25.8-km-wide impact crater Taussig at lat 9.2° S., long 229.0° E. Helen Brooke-Taussig (1898–1986), after whom the crater is named, was an American physician known for saving the lives of babies with heart and blood circulation problems (“blue baby” condition). Along with Alfred Blalock she developed the Blalock-Taussig operation that saved many “blue babies” from invalidism or death.

V–39 is 2,632.2 km north-south by 3,158.6 km east-west and has an area of 8.10×10^6 km^2. It is bounded by Atla Regio to the northwest, Ulfrun Regio to the north, Wawalag Planitia to the south, and Hinemoa Planitia to the northeast. It contains 13 impact craters, 4 large volcanoes, 8 paterae, 24 coronae, a 3,900-km-long section of the Parga Chasmata rift system, and parts of Hinemoa and Wawalag Planitiae (fig. 1). Elevations within the area vary from 4.3 km above to 3.6 km below the mean planetary radius (MPR, 6,051.84 km, fig. 2; Pettengill and others, 1992). Emissivity values within the quadrangle (fig. 3) vary from 0.52 to 0.95 with the average 0.85

(similar to the mean emissivity of 0.845 for the Venusian surface [Pettengill and others, 1992]). A dichotomy in values appears to exist between the materials northeast of the Parga Chasmata rift system (for example, units pl, puT, pf, fC_2, and fM_1) and those to the south (for example, units prT, pli). This dichotomy is most likely attributed to separate plains and volcanic flow materials that contain minerals with different dielectric constants.

Previous analyses within the Taussig quadrangle have mainly focused around coronae. Various studies have included the identification and classification of coronae (Stofan and others, 1992), the tectonic and volcanic characteristics of Parga Chasmata (Hamilton and Stofan, 1996), and the formation, evolution, and deformation of coronae along its length (Stofan and others, 1993; Stofan and others, 2000b; Ghail, 2001). Using gravity data, Schubert and others (1994) calculated apparent depths of compensation of 75–200 km for several coronae along Parga Chasmata, although most were found to have no resolvable signature. Gravity/topography admittance observations (Stofan and others, 2000b; Anderson and Smrekar, 2000) have also been used to suggest a delaminating lower lithosphere beneath Parga coronae, which helps to explain their topographic shapes.

MAPPING TECHNIQUES

Standard mapping techniques were used to map the geology of the quadrangle (for example, Willhelms, 1972, 1990), taking into account the use and nature of radar images (Ford and others, 1989; Tanaka, 1994). Materials were defined primarily on the basis of their relative radar brightness, surface texture, and stratigraphic position. Cross-cutting and embayment relationships helped to determine the geologic evolution of the area. The problems and pitfalls of interpreting radar images are well known (for example, Ford and others, 1993) and will not be repeated here. Specific problems encountered in mapping this quadrangle are discussed below.

Mapping was undertaken on a 1:5,000,000-scale SAR backscatter photomosaic base prepared by the U.S. Geological Survey (USGS). The majority of the area (97%) is covered by cycle 1 data with many small data gaps filled by right-looking data from cycle 2. The right-looking areas have a darker tone to highlight the difference in look direction and to avoid misinterpretation of the data. In cycle 1 the incidence angles for images taken of the Taussig quadrangle ranged from 44.9°–35.5°; in cycle 2 they ranged from 24.9°–25.1° (Plaut, 1993).

The SAR data used to help construct the map include compressed once mosaicked image data records (C1-MIDRs) at 225 m/pixel scale and full resolution (F-MAP) images at 75 m/pixel scale, both in digital and photographic form. The F-MAPs, produced by the USGS, allowed the detailed comparison of widely spaced regions at full Magellan resolution and were fundamental to the construction of the map. A synthetic parallax stereo image data set with 10x vertical exaggeration, again produced by the USGS, proved to be invaluable in determining the relationship between map units. Structural and embayment relations are well illustrated in these images, which were of particular use in understanding the complex deformation associated with the chasma regions.

Geologic mapping was assisted by the use of Magellan altimetry, rms slope, Fresnel reflectivity, and emissivity data (Pettengill and others, 1992) prepared by the Massachusetts Institute of Technology and distributed in digital form. These data sets provide additional information on the properties of individual map units (table 1; Campbell, 1995). Three-dimensional perspective renderings were generated for certain features in the area by draping SAR data over digital elevation models (DEMs) using the 3DEM software package (figs. 4, 5). Although the process is subject to artifacts and care must be taken when interpreting the images, it proved a valuable tool for visualizing complex geologic landscapes and the stratigraphy of individual features.

Specific problems that occurred during mapping were mainly associated with determining the absolute boundaries of units. Adjacent materials can only be separated if they have distinctly different radar backscatters from each other. Conversely, surface properties of an individual unit may also change from one area to another, which could lead to it being mapped incorrectly as more than one unit. Digital manipulation of the SAR data and the comparison of different data sets helped to highlight potential mapping errors. Because V–39 is an area containing extensive deformation, it was difficult and sometimes impossible to follow unit boundaries into or across the chasma regions.

UNIT PHYSICAL PROPERTIES

The physical properties of each individual map unit provide information about the characteristics (such as grain size, surface texture, and dielectric constant) of the materials that constitute that unit. Quantitative comparisons between units from different areas of the planet are hampered by the fact that the SAR data were taken at different incidence angles at different latitudes (Plaut, 1993). Comparisons can therefore be achieved once the variation in incidence angle has been taken into account. A software program by Campbell (1995) compensates for this angle and also removes the Muhleman backscatter calibration and calculates the backscatter DN, converting it to a decibel value. The backscatter properties of all plains, volcanic, and corona map units in V–39 are shown in figure 6.

In deriving these statistics, care was taken to sample a suitably representative area for each unit and to avoid contamination of the selection by other units, unrepresen-

tative structures, or data gaps. Single boxes were used for each unit, although some materials were hard to define, because the backscatter properties are affected by the density of associated fractures. Although this information can contribute to determining the properties, and even the most likely origin of the unit, and was referred to when constructing the map, the central method of mapping was based upon the visual properties of the SAR images.

MATERIAL UNITS AND VOLCANIC LAND FORMS

Plains Materials

Ten distinct plains materials are identified within the quadrangle based on morphologic and stratigraphic relationships: densely fractured plains material (unit pdf), hilly plains material (unit ph), lineated plains material (unit pli), shield plains material (unit psh), fractured plains material (unit pf), Taussig uniform plains material (unit puT), lobate plains material (unit pl), undulating plains material (unit pu), Taussig regional plains material (unit prT), and smooth plains material (unit ps). Each plains unit has formed over time during episodes of resurfacing, and each unit has been interspersed with periods of regional or local extension or compression. At the highest image resolution, some materials (for example, unit prT) appear to be composed of numerous small-scale flows having similar radar backscatter, which suggests that they have built up over time from a variety of different sources. The scale of each of these plains units varies from <100 km^2 to >100,000 km^2.

Densely fractured plains material (unit pdf; for example, lat 23.5° S., long 222.5° E.) occurs throughout the quadrangle. It has strong radar backscatter coefficients that represent highly deformed material with very rough surfaces. All the outcrops consist of inliers rising above the surrounding materials, which embay them. Most blocks are 50–75 km across although some may be slightly larger. Some unit pdf material shows multidirectional deformation, but no dominant trends are observed within the quadrangle. The unit is embayed by eighteen different units, but there is no evidence to suggest all unit pdf materials are the same age or of the same origin over the whole of the quadrangle. The material is interpreted to be volcanic plains that have been highly deformed and (or) possibly the high-standing rims of old coronae.

The hilly plains material (unit ph), west of Maram Corona (for example, lat 7.0° S., long 215.5° E.), is characterized by a moderately high backscatter coefficient. The northern part of the unit is heavily deformed by northeast-trending ridges and fractures associated with the Veleda Linea branch of the main Parga Chasmata rift system. The southern part of the unit is generally more homogeneous, having finer, less closely spaced north-south lineaments. The unit is superposed by all surrounding materials including lava flows from Maram and Ya-Yerv Coronae and the lineated plains material (unit pli) to the south.

The lineated plains material (unit pli) generally has intermediate to low backscatter. Its morphology is largely characterized by multidirectional linear and curvilinear fractures and ridges associated with corona uplift and formation (for example, Onenhste Corona [lat 19° S., long 221° E.]). The unit is also cut by northwest-southeast-trending fractures associated with the Parga Chasmata rift system. The material is surrounded by both younger (unit prT) and older (units ph and pdf) plains materials, is postdated by many volcanic center and corona materials, and has a spread of ages throughout the stratigraphic column.

Shield plains material (unit psh) is in the northern part of the quadrangle. It is high-standing in relation to surrounding units and has a high backscatter coefficient. It is characterized by a concentration of small volcanic edifices, predominantly shields (<5 km diameter), and could represent older widespread edifice field material. The material shows a moderate amount of deformation, mainly from north-northeast-trending fractures and lineaments. The small edifices both predate and postdate the fracturing, which indicates that deformation occurred throughout edifice formation.

Fractured plains material (unit pf) has an intermediate backscatter coefficient and is characterized by north-south-trending fractures and lineaments. This highly deformed unit is high-standing in relation to surrounding materials (units pl, fL, fI, fLe$_1$, fM$_1$, ef) that embay it. Plains units pdf and psh predate unit pf. Small volcanic edifices are scattered throughout the unit and both postdate and predate the deformation.

Taussig uniform plains material (unit puT) has a constant, unvarying radar backscatter and occurs within the northeastern part of the map area. It contains very little evidence of tectonic disturbance, with the largest concentration of deformation occurring in the southern part of the unit. The margins of the unit are mainly lobate, but some small-scale interfingering is visible with the adjacent lobate plains material (unit pl). The unit is superposed by volcanic center material (unit vc) and isolated flow material (unit f), but it surrounds small outcrops of densely fractured plains material (unit pdf). In some places unit puT is similar in radar backscatter appearance to the Taussig regional plains material (unit prT). As the two units do not come into contact, it is not clear whether they are the same age or indeed the same unit. They have therefore been mapped separately as two distinct units.

The lobate plains material (unit pl) is in the northeastern part of the quadrangle. It consists of low to intermediate backscatter material with some mottling of backscatter on a small scale. The unit has lobate boundaries, and its distribution is topographically controlled in places.

Small- to intermediate-size volcanic edifices and coronae within the unit may have contributed to its construction. Very little deformation is present apart from several widespread lineaments near Parga Chasmata and a more condensed area of fractures and ridges to the northeast. Unit pl material embays the adjacent Taussig uniform plains material and small areas of unit pdf. The contact with the Taussig regional plains material is masked partly by later volcanic flow materials and rifting associated with the chasmata. Where the contact is distinct, unit pl is embayed by unit prT.

Undulating plains material (unit pu) is restricted to the southeastern part of the map area. It has a low to intermediate radar backscatter and is characterized by shallow, rolling topography. A north-south-trending arm, Thaukhud Linea, of the Parga Chasmata rift system heavily deforms one area of the unit along with Samsing Corona flow material (unit fS). High-standing kipukas of unit pdf are surrounded by the unit, which is in turn embayed by unit prT and by Fedchenko Patera flow material (unit fF).

The Taussig regional plains material (unit prT) is the most extensive plains unit in the area, covering approximately 30 percent of the quadrangle. It is characterized by low backscatter coefficients, with small-scale variations in backscatter visible throughout. Some individual flows can be recognized within the unit at F-MAP scale, which suggests that unit prT material could be a collection of many volcanic flows having similar radar backscatter. The unit contains many deformational structures, including two separate major branches of the Parga Chasmata rift system. Widespread northeast-trending wrinkle ridges are also visible in the southeastern area of the unit, which indicates additional late-stage compressional deformation. Unit prT embays several other plains materials, including units pli, pl, and pu. Volcanic flow material from volcanoes (units fL, fG, fMa, fF, fT, vc) and from coronae (units fNd, fA_1, fA_2, fAt, fH) within the unit are superposed on it.

The smooth plains material (unit ps) is only in the southern part of the quadrangle, emanating from an area south of the map area. The unit has very low radar backscatter coefficients and contains a few small edifices (<10 km diameter). Northeast-trending wrinkle ridges also can be seen, indicating late-stage deformation by compressional stresses. The material embays the Taussig regional plains material (unit prT), kipukas of densely fractured plains material (unit pdf), Emegelji Coronae material (unit fE_1), and Villepreux-Power Patera material (unit fV) but is overlain by flows from Fedchenko Patera (unit fF).

Volcanic Materials

V–39 contains a plethora of volcanic materials, including small (<10 km diameter) edifices (cones, shields, and domes) and edifice fields, intermediate (10–100 km) and large (>100 km) volcanoes, rift-associated flow material, and large volcanic flow fields (fluctūs). These units occur throughout the quadrangle, and an analysis of cross-cutting relations shows a variety of unit ages. The unit descriptions below are generally described from oldest to youngest with some exceptions in order to discuss the different unit groups more cohesively. The Correlation of Map Units should be consulted for a more accurate representation of relative stratigraphic ages.

Materials of Volcanic Centers, Paterae, and Large Volcanoes

Twenty-four volcanic centers (unit vc) are present throughout the quadrangle. Each center consists of an intermediate-size central volcanic edifice (typically 10–50 km in diameter) surrounded by an apron of flow material that varies in extent from the source vent (the average flow apron diameter is approximately 80 km). Radar backscatter varies amongst individual units and in places within a center itself. Individual flows can be seen within some centers, which allows the mapping of flow direction. The central edifice may display a summit pit or a caldera of variable size. In most cases, unit vc superposes surrounding plains materials (units prT, pl, puT, pli) but is embayed by flows from local edifice fields (unit ef) and fluctūs (unit fI). As unit vc is made up of materials from many individual sources, it shows a range of ages throughout the stratigraphic column.

Included in the volcanic center category, mapped as symbols and as unit vc, are twelve domes that have various steep-sided (or "pancake") to scalloped-margin morphologies. The steep-sided domes have a range of sizes from 18–125 km and typically appear clustered together (for example, at lat 22.5° S., long 215° E.). Some exhibit pits at their centers and show smooth to highly fractured summit regions. They have been interpreted as being produced by the eruption of high viscosity lavas (Guest and others, 1992; Pavri and others, 1992; McKenzie and others, 1992), such as silica-rich dry rhyolite. However, Fink and others (1993) explain that the domes' high aspect ratios are a feature of episodic rather than continuous eruptions, an uncharacteristic feature of silicic lavas. Stofan and others (2000a) show that at normal Venusian surface temperatures, rhyolitic lavas would quickly form thick crusts that would break into large blocks and be difficult to anneal. The study of steep-sided basaltic domes on the terrestrial seafloor suggests that their morphology can be dominated by eruption conditions rather than composition (Bridges, 1995). Therefore, unless Venus has undergone large temperature excursions in the past (for example, conditions of 800–1,000 K), the eruption of basaltic lavas is suggested to produce the observed morphology (Stofan and others, 2000a).

Scalloped-margin domes within V–39 are generally smaller in diameter and display characteristic radial "fluting" (Guest and others, 1991, 1992). Guest and others

(1991, 1992), Bulmer and Guest (1996), and Bulmer (1994) interpret these features to be formed as a result of the collapse of the margins of initially circular steep-sided domes. Head and others (1992) suggest that some of the fluting may represent rift zones linked to radial dike intrusion.

The quadrangle contains eight paterae that vary in caldera size from 40 km to 160 km. The most prominent of these are Ledoux (unit fL), Jotuni (unit fJ), Villepreux-Power (units vV and fV), and Malibran Paterae (unit fMa). Ledoux consists of a 40-km-wide circular caldera within the main Parga Chasmata rift zone. It is surrounded by an irregularly shaped radar bright flow apron extending up to 400 km from the central vent. Some flows to the far east and southwest of the center have a radar-dark appearance and a sinuous morphology. Some show evidence of being channel fed. The flow apron both postdates and is cut by through-going fractures associated with the rift. Ledoux Patera flow material (unit fL) postdates all other surrounding units including Maram Corona flow material (unit fM), the Taussig regional plains material (unit prT) and the lobate plains material (unit pl), and undifferentiated corona materials (units cu_1 and cu_2).

The calderas characterizing Jotuni and Villepreux-Power Paterae are oval in shape and approximately 160 km x 120 km in size. They have similar morphologies, which display flat, uniform backscatter crater floors surrounded by concentric rings of fractures that characterize the walls and rim of the caldera. Intermediate backscatter lava flows are visible to the north of Jotuni (unit fJ) and are interpreted to have been erupted from the northern rim. They embay unit fC_1 material. Although of little relief, the caldera controls flow material from Ya-Yerv Corona (unit fY_2), which subsequently embays the Jotuni flow material. The floor of Villepreux-Power Patera is covered by radar-dark lava flows (unit fV) that have embayed the northwest rim of the caldera (west of the map area) and also the local plains material (unit prT). The eastern, more visible part of the rim (unit vV), is marked by arcuate fractures and is embayed by flow material from Emegelji Coronae (unit fE_1) and plains units prT and ps. Several small edifices are seen in the center of the patera. Malibran Patera, at lat 18.5° S., long 224.7° E., has a 55-km-wide shallow depression at its center, which does not have a well-defined structure but most likely represents a volcanic caldera. Malibran is surrounded by a diffuse, intermediate to radar-dark apron of deposits (unit fMa), which overlies the lineated and Taussig regional plains material. This apron is also cut by widely spaced fractures and several grabens that are mainly oriented in a northwest-southeast direction parallel to Parga Chasmata to the northeast.

The other paterae vary in size up to 140 km across but they lack the large-scale associated flow apron of Ledoux. They are typically circular or near circular, with flat floors and caldera walls often marked by concentric rings of fractures. They show very little relief, but in places can be seen to control younger lava flows. All the other paterae are within the plains (units pl, prT, and puT) and from cross-cutting relationships can be seen to superpose units puT and prT, but in some areas are embayed by unit pl.

Large volcanoes are classified as volcanic edifices having flow apron diameters of 100 km or more (Head and others, 1992). V–39 contains four named large volcanoes (Mbokomu Mons, Gwen Mons, Toma Mons*, and Fedchenko Patera), although some other volcanic centers also have flow aprons wider than 100 km. Mbokomu Mons sits on the Jokwa Linea branch of the Parga Chasmata rift system. Its main edifice is 240 km wide and at its highest point reaches 1.2 km above the surrounding plains. Its shape is not typical of other classic Venusian large volcanoes (for example, Sif, Sapas, or Gula Montes) but does show some similarities to features such as Sappho Patera and Anala Mons. The central edifice has slopes of a few degrees and is surmounted by a circular depression that drops to 400 m below the height of the rim. This depression does not show the characteristic steep inner walls of a typical caldera but may be a result of relaxation of the magma chamber beneath the main cone. The outer scarps surrounding the edifice are most extensive on the northeast and southwest sides, trending with the direction of Jokwa Linea.

An apron of Mbokomu Mons flow material (unit fMb) extends out to 300 km from the center of the volcano and displays shallow flank slopes of generally less than 1°. Some individual flows travel up to 600 km from the center. The apron is constructed of variable backscatter, but predominantly radar dark lava flows that have a dendritic morphology. The outer, more extensive flows have a very dark, uniform backscatter and could represent an earlier eruptive episode. Most flows appear to have emanated from the center of the volcano, but there could be additional flows erupted from several large grabens around the flanks of the main edifice. Unit fMb postdates plains units pdf and pli and embays corona units cR, fR_1, fR_2, fY_1, and cu_2. The summit of Mbokomu is characterized by radial fractures and grabens confined mainly to the central edifice. The outer apron shows very little tectonic deformation and postdates all other local units in addition to the rift. The shape and summit characteristics of the volcano have led to Mbokomu being classified as both a large volcano (Head and others, 1992; Crumpler and others, 1997) and a corona (Stofan and others, 1992). Several features on Venus have morphologies transitional between coronae and large volcanoes, which leads to confusion over their geologic histories and origins (Herrick

*Provisionally approved by International Astronomical Union

and McGovern, 2000; Stofan and others, 2002). Mbokomu may be classified as one of these "hybrid" features but until further investigations reveal why differences in morphology occur, we are treating Mbokomu as a large volcano, as it has been named as such.

Fedchenko Patera flow material (unit fF) lies along the southern boundary of the map area. The volcano has a broad, low relief, rising only 500 m at its highest point above the surrounding plains. The summit structure consists of a 46-km-wide caldera marked by a concentric ring of fractures. The caldera appears to be filled by radar-dark lavas that have almost breached the southwest rim. A steep-sided dome and a semi-circular-shaped collapse feature lie within a ring of fractures that surround the main caldera. This larger ring may represent an older, filled caldera complex. The flow apron surrounding Fedchenko is made up of both lobate and digitate flows. Small edifices are scattered throughout the apron and may be representative of flank eruptive vents. A radar bright flow to the north of the caldera is topographically controlled by an adjacent area of high-standing lineated plains material. Fedchenko Patera flow material (unit fF) postdates the emplacement of the lineated, Taussig regional, undulating, and smooth plains units.

Gwen Mons (lat 21.2° S., long 238.7° E.) lies in the far southeast corner of the map area. It is a simple cone-shaped edifice reaching a maximum height of 800 m above the surrounding plains. The main topographic edifice is 70 km in diameter and is surrounded by a flow apron (Gwen Mons flow material, unit fG) extending up to 100 km from the center. The volcano is superposed on a set of east-west-trending fractures most likely associated with the Parga Chasmata rift system 200 km to the north. The flow apron has intermediate backscatter, similar to the surrounding Taussig regional plains material (unit prT), but some individual flows can be recognized. Part of the summit region and the northern flank is obscured by a data gap, but an 8-km-wide circular collapse feature can be seen offset from the center, possibly indicating the presence of a caldera complex. Unit fG material postdates unit prT.

Toma Mons is the source for a mainly diffuse, radar-dark, elongate flow apron (Toma Mons flow material, unit fT) centered at lat 12.8° S., long 231.9° E.. The main edifice has a topographic diameter of 90 km but reaches a maximum height of only 500 m above the surrounding plains. The flow boundaries are less defined around the southern part of the unit but appear to terminate at the edge of Dziwica Chasma. Several fractures and lineaments, oriented parallel to Dziwica Chasma, cut the flows, but it is not clear whether the main part of the chasma was formed before or after their initial emplacement. A circular, diffuse, radar-bright area of materials (also mapped as unit fT) also surrounds the main topographic summit. Unit fT overlies fractured and Taussig regional plains materials and embays Lumimuut Corona flow material (unit fLu) to the northeast and edifice field material (unit ef) to the west. Flow material (unit vc) sourced from an intermediate-size volcanic center embays unit fT to the west.

Clusters of small edifices are common throughout the quadrangle, and many clusters are surrounded by associated lava flows. Edifice field material (unit ef) tends to have diameters of 50–100 km, but some are more extensive, up to 300 km across. The unit is mapped on the assumption that the edifices contained within the field share a common source and (or) are stratigraphically related. A typical number of edifices for a field is approximately 50. Each small edifice symbol mapped within unit ef represents 5–10 single edifices. In many areas the field is surrounded by an apron of flow material having distinct boundaries, which may extend as far as 150 km from the center of the field. These materials have a variable radar backscatter, but in many areas are radar dark, which indicates a smooth surface texture.

Edifice fields are defined as regions of small volcanoes in which there are higher concentrations than the regional average density, which ranges from 4–10 per 103 km^2 and numbers ≥100 within a generally equant area ≥100 km in diameter (Aubele and others, 1992). Volcanic constructs within edifice fields show a range in morphology (Guest and others, 1992) but are generally topographically low (slopes less than 5°) and are typically surmounted by a pit (Aubele and Slyuta, 1990). Edifices associated with areas of fracturing have elongated summit pits oriented in a similar direction to that of the fractures.

Where some edifice field material in V–39 is embayed by smooth plains material (unit ps), patches of isolated flow material (unit f), and several corona and volcano units (units fY_2, fM_1, and fV), the majority postdate the materials that surround it (units pdf, pli, prT, puT, pf, pl, fC_1, fR_1), indicating its youthfulness. Similar observations are seen in other quadrangles (for example, at Olosa Colles in V–31 [D.L. Copp, oral commun., 1997]). Crumpler and others (1997), following a study of 647 shield fields, found that although enhanced small volcano formation may have occurred at some time or in some regions, small volcano formation did not occur planetwide as a single event.

Many volcanic features and flows are associated with the Parga Chasmata rift system in V–39. These include small volcanic shields, cones and steep-sided domes, shield volcanoes (for example, Mbokomu Mons), large paterae and calderas (for example, Ledoux Patera), flows associated with coronae, and fractures associated with lava flows. Flows that originate directly from the rift are mapped north of Maram Corona. This Parga Chasmata flow material (unit fP) has a sheetlike morphology and high backscatter. Unit fP appears to emanate and flow northward away from the

northern margins of Kicheda Chasma (northwest corner of map area, fig. 1). Other rift flows are observed originating from the northern margins of Lesavka Chasma (northwest corner of map area, fig. 1). Because the density of tectonic deformation in these regions is very high, it is often difficult to associate an individual flow to a particular source. Therefore, the amount of volcanism directly attributable to rift construction and development may well be underestimated. What is evident is that these flow materials both cut and are cut by rift-associated fractures, which indicates that volcanism and tectonism have occurred throughout the history of the rift.

Patches of isolated volcanic flow material (unit f) are present within the quadrangle. They typically show little variation in their backscatter, although different flows can appear radar bright or dark, which indicates variations in surface roughness. Source vents for these materials are small pits or fissures; some flows occur within part of the Parga Chasmata rift system. Isolated flow material is usually less than 75 km in length, although some longer flows are observed in the northern part of the map area. Most isolated flow material overlies other units, indicating that they are younger. Some show varying amounts of tectonic deformation and therefore may not be limited to the youngest epoch. The material is interpreted to be the manifestation of local areas of melting below the crust, which produced volcanoes lacking edifices. The lavas erupted may have a low viscosity therefore inhibiting edifice construction.

Two large flow fields are mapped within V–39. The largest, Itoki Fluctus material (unit fI), covers an approximate area of 20,000 km^2 and is almost 900 km long. No apparent source vent is visible, although many small edifices are scattered throughout the unit. Itoki has a variety of radar backscatter coefficients and displays a streamlined morphology, including the presence of several sinuous streaks or channels. The margins of the unit are lobate. Low radar backscatter flows surround a large high backscatter region (approximately 8,000 km^2 in size), suggesting that later, more fluid lavas have lifted up the rough, broken crust of an earlier flow and spread out from its edges. The flow field is cut by very few lineaments and postdates all materials adjacent to it.

Ningyo Fluctus material (unit fN), in the northwestern corner of the map area (lat 4.5° S., long 210.5° E.), has a source to the west of the quadrangle from an area of fractures and large grabens about 900 km south of Ozza Mons. The flow field is approximately 970 km long although only 190 km is seen within V–39. It has a very high radar backscatter and has flowed into the central depression of an old corona-like structure (unit cTd) that had earlier been embayed by Chantico Corona flow material (unit fC$_1$).

Other great flow fields are seen elsewhere on the planet, for example, Neago Fluctus in V–19 (Lancaster and others, 1995; Copp, 1997) and Mylitta Fluctus in V–61 (Roberts and others, 1992), and are interpreted as extensive volcanic flow materials with an area greater than 50,000 km, commonly associated with rift zones (Guest and others, 1992; Head and others, 1992; Lancaster and others, 1992, 1995). This observation strongly indicates conditions of lithospheric thinning. Crumpler and others (1997) found that 54 percent of large flow fields are within the BAT (Beta-Atla-Themis) zone. Flow fields on Venus have been compared to large terrestrial flows. Typical effusion rates are estimated as between 10^4 and 10^6 m^{3}s^{-1} with a days-to-months typical duration (Roberts and others, 1992). These values are similar in size and volume to at least one flow unit in the Columbia River Basalt Group (Swanson and others, 1975; Shaw and Swanson, 1970).

Corona Materials

Twenty-four coronae are present within V–39 quadrangle; they range in diameter from 100 to 600 km (table 2). In addition, flow units associated with four coronae centered outside the area (Kolias to the west, Lengdin to the north, and Atete and Dhorani to the east) are also mapped. Fourteen of the coronae in the region have identifiable and mappable units that are interpreted to be volcanic in origin. The majority of the coronae have been categorized by Stofan and others (2001b) as concentric types, several with double rings and others as multiple or asymmetric. They are found in two main geologic settings: those formed within the plains and those formed on or within the rift. Nine coronae are associated with plains and fifteen are associated with the Parga Chasmata rift system. The four coronae outside the map area are also associated with segments of Parga. The unit descriptions below are generally described from oldest to youngest with some exceptions in order to discuss the different unit groups more cohesively. The Correlation of Map Units should be consulted for a more accurate representation of relative stratigraphic ages.

Plains Corona Materials

Six plains coronae have mappable deposits, whereas the other three are simply structures that deform the local plains. All are identified as topographically raised, quasi-circular structures marked by varying amounts of concentric and radial fractures. Inacho Corona displays a topographically uneven interior encircled by an outer rim. The rim is marked with concentric fractures, and radial lineaments extend out from this annulus. Flow deposits, Inacho Corona flow material (unit fIn), are particularly evident in the center of the corona and emanating from the western portion of the rim. Clusters of small edifices are associated with flows within the center and also around the northwestern part of the corona. These flows postdate

the majority of internal and external fracturing, which suggests that the volcanism associated with Inacho did not occur in one single event. It is not clear whether Inacho is composed of flow material associated with the formation of the corona or if it is an older uplifted or high-standing plains unit. The corona is postdated by flows from Rzhanitsa Corona (units fR_1 and fR_2) to the north and Emegelji Corona (units fE_1, fE_2) to the southeast.

Lumimuut Corona is made up of two units: Lumimuut Corona material (unit cLu), which is highly deformed, and Lumimuut Corona flow material (unit fLu). The highly deformed material makes up a semi-oval raised rim marked by a high degree of concentric fracturing. This fracturing may represent either uplifted older plains or early-stage Lumimuut Corona flow material. The flow material surrounds the rim to the north and embays it along the eastern side, flooding the interior. Several small shields occur within the center of the corona, and these may have contributed to this volcanic material. Unit cLu is also embayed to the south by the lobate plains material (unit pl). The flows from Lumimuut postdate unit pl, which indicates that the corona has had a protracted history. Flow material from two adjacent volcanoes (Toma Mons, unit fT, and a volcanic center, unit vc) embays both unit cLu and unit fLu.

Tadaka Corona (unit cTd) is defined by high-standing arcuate material interpreted to be the remnants of older uplifted plains or early volcanic materials associated with the formation of this structure. It has been embayed by later materials (for example, volcanic flows from Ningyo Fluctus (unit fN) pond within a depression partially encircled by unit cTd) that postdate its formation.

Adjacent to Inacho Corona is Emegelji Corona, which consists of two semicircular rim segments each defined by concentric sets of fractures. It has been mapped as one feature although it could be a double or two individual adjoining coronae. A 120-km-wide depression lies between the two rims and is partially embayed by lava flow materials, Emegelji Corona flow materials (units fE_1, fE_2). Its center is covered with radar-dark material, and the feature could have been the source for earlier volcanic flows. Two flow units associated with the corona have been mapped (units fE_1, fE_2). The earliest material, unit fE_1, extends out to the northeast and southwest and postdates units prT, pdf, and fR_1. Unit fE_1 is embayed by unit ef and by flows from Inacho Corona (unit fIn). The youngest flows, unit fE_2, are predominantly radar dark and mainly ponded within the two corona rims; they also postdate unit fE_1.

Onenhste Corona also has a complex history. It is oval in shape and is marked by a shallow topographic rim. The interior is slightly domed with the majority of topography offset to the west of the center. The central area of the dome displays a circular depression containing a cluster of small volcanic edifices. This area appears to be the source of a radar-dark flow unit, Onenhste Corona flow material (unit fOn), that embays much of the associated fracturing around the western half of the corona. Onenhste is marked by concentric and radial fractures that extend out into the surrounding plains. The eastern rim is most heavily deformed.

Onenhste deforms unit pli and therefore postdates it. These plains are deformed by the radial and concentric fractures. Several units (unit prT, ef, cu_2) truncate much of the radial deformation where they embay unit pli. However, other radial fractures cut these units, which indicates that there have been at least two stages of deformation (possibly associated with secondary uplift of the corona) over the evolution of the feature. The secondary fracturing also cuts unit fOn, suggesting that this deformational event occurred after unit fOn emplacement.

Rift Corona Materials

Many circular or quasi-circular tectonic features are associated with the rift system in V–39. Fifteen individual rift coronae have been identified and eight of these have mappable associated volcanic deposits. They vary in diameter from 150 km (Chantico) to 600 km (Maram). All these coronae have geologic histories tightly bound to the formation of the rift, and many show complex and protracted evolutions. Fracturing and other tectonic deformation plays a large part in coronae formation (Stofan and others, 1992), which, combined with the tectonic extension associated with the rift zone, make it difficult to reliably distinguish all volcanic deposits and coronae structure with these particular features.

Rzhanitsa Corona is southwest of Mbokomu Mons on the Jokwa Linea branch of the Parga Chasmata rift system. It has an elongate appearance and has been highly deformed by fractures and grabens trending mainly along the direction of this fracture zone. A tear drop-shaped ring of concentric fractures mark out a shallow rim, and radial lineaments, mainly grabens, extend out along the flanks. The interior of the corona, mapped as Rzhanitsa Corona material (unit cR), has been embayed in parts by radar-dark lavas, and several steep-sided domes and small shields have formed along its length.

Two flow units have been identified around Rzhanitsa. Rzhanitsa Corona flow material, member 1 (unit fR_1) has radar-dark backscatter and embays units pli and prT and Inacho Corona flow material. It is postdated by Rzhanitsa Corona flow material, member 2 (unit fR_2), which has a more mottled appearance, and also by flow material from Emegelji Corona (unit fE_1). Flows from Mbokomu Mons (unit fMb) postdate all Rzhanitsa units. Units fR_1 and fR_2 both embay and are cut by fractures along the rift, which indicates that deformation and volcanism in this area have overlapped in time.

Chantico Corona, within the main rift system, has a similar morphology to Oduduwa and Ya-Yerv Coronae.

It has a summit plateau surrounded by steep scarps that form the walls of the Lesavka and Kicheda canyons. The interior is marked by concentric and through-going fractures associated with the rift. There appears to be little radial fracturing emanating from the center of the plateau. A radar-bright flow field, Chantico Corona flow material, member 1 (unit fC_1), surrounds the corona mainly to the south and embays adjacent coronae, including Pazar-ana, a 300-km-wide corona to the south. A radar-dark flow apron, Chantico Corona flow material, member 2 (unit fC_2), extends up to 500 km from the center of Chantico. This field embays many local features but in parts is highly deformed by fractures and rifting associated with Parga Chasmata. A large area of overlapping flows having various radar backscatters lies to the west of the corona. These flows are mapped as part of unit fC_1 and are attributed to Chantico, although they probably include other flows from nearby coronae (for example, Attabeira) and lavas erupted from the rift.

Oduduwa and Ya-Yerv Coronae sit adjacently on the Veleda Linea section of the Parga Chasmata rift zone. They have similar morphologies, both with circular, plateaulike centers surrounded by steep scarps. Oduduwa displays more concentric deformation than Ya-Yerv around its plateau and has a highly deformed ridge and trough system around the southern side. The central area of Oduduwa has been mapped as Oduduwa Corona material (unit cO). Both coronae have highly fractured interiors with grabens radiating away from their centers. They have previously been classed as large volcanoes with stellate fracture centers (Crumpler and others, 1997) and also as coronae (Stofan and others, 1992). Both features show similarities in morphology to Mbokomu Mons and appear to be transitional between coronae and large volcanoes. Further investigation is needed to determine why these differences occur, but for the purposes of this study both features are treated as coronae.

Oduduwa and Ya-Yerv Coronae have extensive volcanic deposits with varying radar backscatters and individual flows with dendritic morphologies. These flows postdate the majority of rifting. The deposits at Oduduwa, Oduduwa Corona flow material (unit fO), appear to emanate from around the annulus, whereas many flows from Ya-Yerv, Ya-Yerv Corona flow material (units fY_1 and fY_2), can be traced to its center. An earlier flow deposit, Ya-Yerv Corona flow material, member 1 (unit fY_1), indicates more than one stage of volcanism. It is postdated by the later flow unit fY_2 and by unit fO. Ya-Yerv Corona flow material, member 2 (unit fY_2) is the youngest of the two features, embaying fO material to the north of the coronae centers.

Maram Corona is the largest corona in V–39 and has three mapped units, Maram Corona flow materials, members 1 and 2 (units fM_1 and fM_2), and Maram Corona volcanic center material (unit vcM). It has an oval-shaped plateau structure surrounded by an annulus that varies in topography and tectonic deformation. The north side of the annulus forms part of the chasm walls of Kicheda Chasma and displays extensive ridge and trough topography. The west and east sides are less fractured and show narrow grabens and shallower topography. The south side is characterized by an arc-shaped segment of annulus with an outer scarp. An area of highly deformed radar-bright material on the south side of this segment could represent an older, partially embayed part of the annulus. Several large grabens cut across the lower central part of the plateau and extend out into the rift system. The plateau is tilted along its east-west axis with the north rim standing 2.3 km higher than the south rim. This uplift is interpreted to have occurred during the formation of the rift, which indicates that Maram was in at least its early to middle stages of development when large-scale faulting occurred.

The flow units associated with Maram have all been deformed by the tectonics of the rift. The earliest deposits (unit fM_1) make up an apron of radar-dark lavas that extend up to 600 km from the center of the corona. They are more extensive on the west and southwest sides of the corona and display individual flow fronts within the field. This unit postdates units ph and pli to the west, unit pf to the northeast, flows from Lengdin Corona (unit fLe_1), a small shield field, and volcanic center material. It is embayed by lava flows from Ledoux Patera (unit fL) to the southeast and is severely deformed by Parga Chasmata, but in some places can be traced through the rift.

Unit fM_2 is radar dark and displays distinct dendritic flow fronts that have variable backscatters. It embays unit fM_1, but is embayed by unit fL and is cut by the rift and annulus. Much of the north half of the unit boundary is difficult to discern owing to the severe deformation associated with the rift. The interior of the corona is characterized by a volcanic center, mapped as Maram Corona volcanic center material (unit vcM). Some later, radar-bright flows associated with this center flow upslope of the vent, indicating that they were emplaced before major uplift of the corona occurred. These volcanic flow materials (unit vcM) embay unit fM_2 and are cut by radial fractures and grabens.

Maram shows morphological similarities to other large coronae along neighboring chasmata systems. Atete Corona in V–40, Zisa and Lengdin Coronae in V–27, and Taranga Corona in V–28 are all over 500 km in diameter and display elongate plateaulike shapes. Each of their flanks is bounded in part by sections of rift troughs, and each plateau is surmounted by a radially fractured volcanic center. These large features have been suggested to represent structural barriers to trough propagation (for example, Hamilton and Stofan, 1996; Chapman, 1999).

Samsing, Ndoi, and Aeracura Coronae each display rings of concentric fractures that mark out their tectonic

annuli. The fractures coincide with their raised outer rims, although Ndoi has an additional second outer ring of fractures to the west. All three coronae exhibit associated lava flows. Aeracura has two associated deposits, Aeracura Corona flow materials, members 1 and 2 (units fA_1 and fA_2). Unit fA_2 postdates unit fA_1 and is confined mainly within the center of the corona. Flows around Ndoi, Ndoi Corona flow material (unit fNd), embay its interior and a shallow arcuate moat around the west side, and radar dark flows, Samsing Corona flow material (unit fS), appear to emanate and flow away from the north rim of Samsing.

We have also mapped two areas of undifferentiated corona materials, units cu_1 and cu_2. The units are south of Maram Corona and east of Mbokomu Mons. Unit cu_1 is composed primarily of an area of arcuate fractures and lineaments named as Ulgen-ekhe Coronae. These fractures most likely represent the deformed annuli of a group of old or partially formed coronae. They are surrounded and embayed by intermediate to radar-dark lava flows interpreted to originate from the formation of the corona structures, and several identifiable flow fronts indicate flow direction. A radar-dark lobe of unit cu_1 embays part of the rim and ejecta blanket (unit c) of Yenlik crater (lat 16° S., long 225.4° E.), giving a stratigraphic marker and suggesting that unit cu_1 is younger than Yenlik. Unit cu_2 is less deformed than unit cu_1 and is interpreted to be younger. It also has a more radar dark appearance and displays lobate boundaries and, in places, well-defined flow fronts. Some material that forms unit cu_2 could originate from Repa Corona (lat 13.0° S. long 218.8° E.) to the north. Unit cu_1 overlies plains units pli and prT and is embayed by units cu_2 and fL. Unit cu_2 overlies plains units pdf and pli and is embayed by flows from Mbokomu Mons (unit fMb) and Ledoux Patera (unit fL).

Materials associated with coronae outside the quadrangle (Atete [unit fAt], Dhorani [unit fD], Kolias [unit fK], and Lengdin [unit fLe_1, fLe_2]) extend into V–39. Flows from Kolias Corona superpose materials associated with Rzhanitsa Corona, and flows from Atete superpose unit prT. Dhorani Corona flow material (unit fD) postdates the lobate plains (unit pl) but is superposed by later volcanic center material. Lengdin Corona flow materials, members 1 and 2 (units fLe_1, fLe_2) resurface the largest area of the four exterior coronae and postdate some older plains (units pf, psh) but are overlain by younger coronae (units fM, fC), Parga (unit fP), and edifice field materials (unit ef).

STRUCTURES

Parga Chasmata Rift System

V–39 is dominated by the complex troughs, ridges, and fractures of the Parga Chasmata rift system. The main region of deformation runs diagonally northwest to southeast through the map area, although several other zones of fractures branch away from the main system. The Parga Chasmata system runs from Ozza Mons (northwest of the map area at lat 4.5° N., long 201° E.) to Themis Regio (at approximately lat 25° S., long 285° E.) roughly 1,900 km to the southeast. It is characterized by linear features including fractures, grabens, normal faults, and contractional ridges. It is not a well-defined rift system, such as Devana or Juno Chasmata, and it displays complex branching networks having several discontinuous offsets along the main system (Stofan and others, 1997). Two distinct morphologies are associated with the main zones of tectonics running through the map area: regions of diffuse fracturing having minor trough development, and regions of dense fracturing having significant trough development. Similar morphologies are seen along the Hecate Chasma system to the north (Hamilton and Stofan, 1996). A broad and diffuse central zone of tectonic faults separates four conspicuous troughs within the quadrangle (fig. 7), two to the northwest and two to the southeast. The four canyons (Chondi, Dziwica, Kicheda, and Lesavka Chasmata) vary in depth to 4.7 km below the local plains, and the rims of the troughs are as high as 3 km above the local plains in places. Kicheda (lat 1.5° S., long 207° E. to lat 2.5° S., long 213° E.; 1,500 km long) and Lesavka (lat 1.0° S., long 212° E. to lat 0.8° S., long 215° E.; 800 km long) are northwest of Maram Corona. The two troughs originate approximately 250 km west of the map area and bifurcate around the high-standing circular plateau of Chantico Corona. Lesavka Chasma terminates at the 110-km-wide depression of Rogneda Patera, whereas Kicheda Chasma trends southeastward and follows an arcuate path around the northern end of Maram Corona, where it terminates. Chondi Chasma (lat 17.0° S., long 226° E. to lat 18.5° S., long 230° E.; 1,000 km long) and Dziwica Chasma (lat 14.0° S., long 228° E. to lat 15.5° S., long 235° E.; 1,300 km long) are in the southeastern part of the map area. They are approximately parallel to each other and are separated by a 450-km-wide band of Taussig regional plains material (unit prT).

Three major arms of fractures branch away perpendicularly from the main northwest-southeast rift zone. All are on the south side of the main zone and extend out into the surrounding plains. Although all three arms display a reasonably high concentration of fractures, none have developed significant trough morphology. The most westerly arm (Veleda Linea) branches off Parga Chasmata at approximately lat 6° S., long 215° E., trends southwest, and terminates at roughly lat 19° S., long 200° E. Two large coronae (Oduduwa and Ya-Yerv) are superposed along its length, both displaying significant flow aprons that postdate the majority of the fracturing. The lineaments contained within this arm are predominantly fractures and grabens, many of which radiate away from the centers of the two coronae. The central arm (Jokwa

Linea) departs from the main zone to the south of Maram Corona (~lat 13° S., long 220° E.). It is very diffuse in morphology and swings away to the west, where it joins Veleda Linea at approximately lat 16° S., long 209° E. Superposed on the branch is the large volcano or corona, Mbokomu Mons. The most easterly arm (Thaukhud Linea) leaves Parga Chasmata at approximately lat 20° S., long 232° E. It runs directly southward and eventually terminates at around lat 33° S., long 239° E. The section within V–39 is characterized by cross-cutting linear and curvilinear fractures that may represent the fracture annuli of less developed coronae. Very few flows are associated with this section of the arm.

The rift system displays a complex geologic history, intertwined with the formation and development of the coronae and volcanoes along its length. The timing of individual tectonic events is unclear, but volcanism and rifting have overlapped in time. The majority of the rifting in the area postdates the formation of the local plains, with subsequent volcano and coronae development along the system (for example, at Mbokomu Mons and Maram Corona) displaying cross-cutting relationships with several generations of tectonic activity. The youngest tectonic events appear to be long (hundreds of kilometers) parallel sets of southeast-trending grabens that run along the main zone. The majority of these grabens cross-cut earlier associated rift flows and fractures.

Fractures and Grabens

The quadrangle contains an abundance of linear features interpreted to have an extensional origin. The majority of these are oriented parallel to the Parga Chasmata rift system. Many are too narrow to distinguish their geometry but some are wide enough to be identifiable as grabens. The most prominent of these features is the 1,700-km-long Penthesilea Fossa that trends southwest across the map area from lat 11° S., long 212.5° E. to lat 21° S., long 229.5° E. These grabens are probably associated with the large-scale extension that defines the Parga rift. Other linear features occur primarily as radial or concentric sets associated with coronae or volcanic centers. The radial sets likely represent surface fractures or narrow grabens overlying dikes derived from the central feature. Similar features are seen in the Spanish Peaks region of Colorado (Anderson, 1951; Odé, 1957; Muller and Pollard, 1977). Virtually all the plains units contain small sets of linear features to varying abundance and degree. The most densely fractured of these is fractured plains material (unit pf) north of the main rift. The plains are elevated regions characterized by a concentration of northeast-trending fractures.

Wrinkle Ridges

Widely spaced, sinuous, radar-bright linear features, interpreted to be wrinkle ridges, are visible within the Taussig regional plains (unit prT) to the southwest. They are characteristically a few to hundreds of kilometers long and have widths of less than about 2 km. The spacing between individual ridges is a few tens of kilometers, and they generally show a southwest-northeast directional trend, running approximately parallel to Jokwa Linea. They have a similar morphology to wrinkle ridges seen in other areas of the planet (for example, McGill, 1994) and also ridges seen on Mars and the Moon (for example, McGill, 1993). Several hypotheses have been suggested for planetary wrinkle ridge formation, including both a structural and volcanic origin (Plescia and Golombek, 1986). Current models suggest they are formed by folding and thrust faulting in response to compression normal to ridge trends (McGill, 1993). The wrinkle ridges in V–39 are younger than the Taussig regional plains material (unit prT), and they likely formed from contractional stresses in the plains as a result of the extension of the rift system. The paucity of ridges in the quadrangle is probably a result of the area being under a largely tensional tectonic regime instead of a compressional one

CRATERS AND SURFICIAL MATERIALS

The 14 mappable impact craters in the quadrangle yield a crater density of 1.6 craters per 106 km^2. This value is below the planetary average of 2 per 106 km^2 (Strom and others, 1994) and is not deemed to be sufficiently statistically different (Herrick and Phillips, 1994) to imply a younger surface age than that predicted by crater densities for the entire planet, 750 Ma (Mckinnon and others, 1997).

The craters range in size from 3.4 to 27.7 km (table 3). Their small sizes inhibit the mapping of individual units within each crater, and, therefore, crater material (unit c) includes the walls, rims, floors, central peaks, and ballistic ejecta associated with each. Crater rims, walls, and ejecta are radar bright, indicating that the surface is rough at the 12-cm radar wavelength scale. They also have a hummocky appearance. Ejecta sheets have irregular to lobate margins and are typically asymmetrical, forming individual arms or lobes. They commonly display a distinct sector where there is an absence of ejecta. This is interpreted to be the result of atmospheric effects induced by the angle of impact, which modifies ejecta trajectories (Schultz, 1992), although partial embayment cannot be ruled out. The floors of all the craters, except Lois (lat 17.9° S., long 214.7° E.), display areas that are radar dark. Some workers have suggested that many dark-floored craters are embayed by external lava flow material (Herrick and Sharpton, 2000). All the dark-floored craters in V–39, except Cortese (lat 11.4° S., long 218.4° E.), Yenlik (lat 16.0° S., long 225.4° E.), and possibly von Suttner (lat 10.6° S., long 234.9° E.), are interpreted to be pristine, and the dark material in their floors is impact

melt produced as part of the cratering process. Cortese exhibits a radar-dark floor that has a similar backscatter to that of the surrounding plains (unit pli). The floor is deformed by several north-south-trending fractures that also cut the local plains. These fractures are associated with part of the Parga Chasmata rift system. Fractures cutting the crater rim or ejecta blanket are not prominent due to their similar radar backscatters. These observations suggest that the impact forming Cortese occurred before, or during, the deformation associated with this part of the chasmata. The ejecta blanket of Yenlik is embayed by radar-dark lava flows associated with a group of coronae to the north (unit cu_1). The flows have breached the crater rim on the southwest side and have embayed the crater floor.

The east side of von Suttner is truncated by a data loss strip in the left-looking radar image but is not covered by right-looking data. Its radar-dark floor appears to have the same backscatter as the surrounding units, but it is not obvious that the crater has been embayed by external lava flows.

Cortese also displays a 25-km-long flowlike deposit extending northward from its continuous ejecta, mapped as crater flow material (unit cf). This unit is interpreted as outflow material and consists of smooth to hummocky material having a variable radar backscatter and a streamlined morphology. Outflow material may include some minor ballistic ejecta blocks and is commonly emplaced as the drainage of fluidized material from the ejecta, typically on the downrange side of the crater (Shultz, 1992; Chadwick and Schaber, 1993; Johnson and Baker, 1994).

Felicia (lat 19.8° S., long 226.5° E.), Seiko (lat 21.0° S., long 216.6° E.) and Yoko (lat 5.7° S., long 232.0° E.) are surrounded by diffuse, low radar backscatter halos. These dark materials are interpreted to be fine-grained debris produced when the surface is crushed by a projectile-generated shock wave (Phillips and others, 1991) and (or) deposition of fine-grained ejecta (Schultz, 1992). The dark materials around Felicia and Seiko are predominantly to the north and south, with slightly higher backscatter deposits visible to the east and west. This orientation is perpendicular to their angles of impact (from the east for Seiko and from the west for Felicia) and may be a similar effect to the origin of radar-dark parabolas seen around other impact craters (Campbell and others, 1992). Some elongation occurs north and south of the deposits around Yoko, but the materials are more uniformly distributed.

A 20-km-wide, radar-dark, circular feature in the north of the map area (lat 2.5° S., long 230° E.) has a diffuse appearance and indistinct boundaries that suggest the materials thin out with distance from the center. It is interpreted to be a "splotch crater" that results from an incoming atmospheric shock wave of a meteoroid that disturbs the surface (Phillips and others, 1991; Ivanov and others, 1992). The bolide may create a crater that is either too small to be detected by Magellan SAR radar or that disintegrates and (or) vaporizes before impact (Schaber and others, 1992; Zahnle, 1992). The size of the meteoroid responsible for these features has been calculated to be a few kilometers in diameter (Zahnle, 1992; Schultz, 1992; Strom and others, 1994).

GEOLOGIC HISTORY AND SUMMARY

The geologic history of the Taussig quadrangle is a complex one that has been dominated by both volcanism and tectonism. A vast array of volcanic and tectonic landforms suggests that these processes have been both repetitive and ongoing. Volcanism has occurred dominantly in the form of volcanic centers, lava flow deposits associated with coronae, extensive lava sheets, and clusters of small edifices. Tectonism has dominated in the form of large-scale extensional rifting, belts of fractures and grabens, clusters of radial and concentric fractures and faults, and small-scale wrinkle ridges.

The oldest visible units in the quadrangle are represented by highly deformed, densely fractured plains material (unit pdf). Other less deformed plains materials (units ph, pf, pli, and psh) embay them and were, therefore, emplaced after unit pdf. The deformation within these plains illustrates that different stress fields acting at different times accompanied or postdated their formation. Deformed plains units were most likely originally formed by volcanism, but it is impossible to determine how long a time period they represent. The grouping of materials having similar characteristics also does not imply that all outcrops are of the same age. There is also little knowledge of their origin. For example, highly deformed fragments of fractured material could be larger pieces of deformed basement (Ivanov and Head, 1996) or parts of old coronae surrounded by younger plains (Hansen and Willis, 1996).

Widespread regional plains materials (units prT, pl, and puT) cover approximately one-third of the quadrangle. At F-MAP scale some individual flows can be recognized, suggesting that these materials could be a collection of many volcanic flows having similar radar backscatters. Regional plains materials in other areas (for example, in Aino and Sedna Planitiae [Stofan and others, 2001a]) show similar patchwork characteristics. The youngest plains material within V–39 is the radar-dark smooth plains material (unit ps) in the southern part of the quadrangle.

Rifting has continued throughout most of the history of the region, overlapping in time with volcano and, more dominantly, corona formation. The density of recent deformation, cutting all but the youngest of units, makes it almost impossible to determine whether rifting began before, during, or after the emplacement of the widespread regional plains materials (units prT and

pl). Tectonic deformation of several earlier plains materials (for example, units pf, psh, and ph) suggests that episodes of crustal extension and compression occurred before the formation of these regional plains. Structural interactions between the large chasmata contained within the rift and some coronae (for example, at Maram Corona and Kicheda Chasma) suggest that at least some of the large-scale rifting and its associated uplift postdated the main stages of corona formation in that area.

Corona formation has occurred throughout the history of the region with coronae forming both within the plains and also associated with the development of the rift system. Most plains coronae formed within the widespread plains materials (units prT and pl), but several formed in older plains units. Multiple episodes of volcanism are observed at several coronae (for example, Oduduwa and Ya-Yerv Coronae), and these overlap with episodes of fracturing associated with the rift. Other features display resurgent volcanic and tectonic activity. Onenhste Corona, for example, shows at least two stages of tectonic deformation truncated by the eruption of lava flow materials. Lumimuut Corona was embayed by unit pl but has since been surrounded by associated flow materials that postdate both it and the lobate plains.

The most recent activity has centered on edifice-forming volcanism (for example, Mbokomu Mons, Ledoux Patera, and Fedchenko Patera) and large volcanic flow fields (for example, Itoki and Ningyo Fluctūs). These materials overlie all units in contact with them and postdate the majority of extension related to the rift system. Some units are still cut by later lineaments, which indicates that the processes of volcanism and rifting have overlapped in time.

Impact cratering has been present throughout the history of the region but provides very little constraint on surface unit ages. The majority of craters mapped within the quadrangle are pristine in appearance and some show radar-dark parabolas. Two impacts, Cortese and Yenlik, have been embayed and deformed by subsequent lava flows and fracturing, giving stratigraphic markers. A mean crater-retention age similar to that suggested for the overall surface of Venus (~750 Ma, McKinnon and others, 1997) seems applicable for this quadrangle.

Two interpretations of the global stratigraphy of Venus have been proposed. The global stratigraphic model of Basilevsky and Head (2000) suggests that landforms on Venus formed during specific periods in a very directional fashion. Guest and Stofan (1999), however, argue for a nondirectional history whereby geologic processes are repeated and not constrained to any particular epoch. Observations of the stratigraphy in the Taussig quadrangle show that similar styles of volcanism and tectonism have occurred throughout the visible history of this part of the Venusian surface. Several episodes of plains formation have resurfaced areas of the quadrangle at different times, and detailed observation suggests that some are constructed of many individual flows. Some coronae have complex, protracted histories intertwined with the units that surround them. This is similar to observations of other coronae studied on Venus (for example, Copp and others, 1998) and contradicts the idealized sequence of corona development suggested in the global model of Basilevsky and Head (2000). Volcanism associated with coronae, large volcanoes, and calderas, as seen throughout much of the stratigraphic column, overlaps with the formation of the widespread regional plains. No evidence exists to suggest that these processes occurred in discrete episodes as suggested by Basilevsky and Head (2000); therefore, this study indicates that the geology of the Taussig quadrangle favors a nondirectional history of evolution (for example, Guest and Stofan, 1999).

ACKNOWLEDGMENTS

We wish to thank Jenny Blue from the USGS for answering our constant requests for new nomenclature, and Duncan Copp and Simon Tapper for valuable and scientifically stimulating discussions. Reviews by Kelly Bender and Victor Baker were extremely helpful. This work was supported by a postgraduate research grant to Antony Brian by the Particle Physics and Astronomy Research Council, a NASA Presidential Early Career Award for Ellen Stofan, and grant GR/01879 to John Guest from the United Kingdom Natural Environment Research Council.

REFERENCES CITED

Anderson, E.M., 1951, The dynamics of faulting and dyke propagation with applications to Britain: Edinburgh, Oliver and Boyd, 206 p.

Anderson, F.S., and Smrekar, S.E., 2000, Venusian coronae with variable elastic thickness as a function of wavelength [abs.], *in* Lunar and Planetary Science XXXI, abstract 1994: Houston, Lunar and Planetary Institute [CD-ROM].

Aubele, J.C., and Crumpler, L.S., 1992, Shield fields—Concentrations of small volcanoes on Venus, *in* International Colloquium on Venus: Houston, Lunar and Planetary Institute Contribution 789, p. 7–8.

Aubele, J.C., Head, J.W., Crumpler, L.S., Guest, J.E., and Saunders, R.S., 1992, Fields of small volcanoes on Venus (shield fields)—Characteristics and implications [abs.], in Lunar and Planetary Science XXIII: Houston, Lunar and Planetary Institute, p. 47–48.

Aubele, J.C., and Slyuta, E.N., 1990, Small domes on Venus—Characteristics and origin: Earth, Moon, and Planets, v. 50/51, p. 493–532.

Basilevsky, A.T., and Head, J.W., 2000, Geological units on Venus—Evidence for their global correlation: Planetary Space Science, v. 48, p. 75–111.

Bridges, N.T., 1995, Submarine analogs to Venusian pancake domes: Geophysical Research Letters, v. 22, p. 2,781–2,784.

Bulmer, M.H., 1994, An examination of small volcanoes in the plains of Venus, with particular reference to the evolution of domes: University of London, Ph.D. dissertation, 430 p.

Bulmer, M.H., and Guest, J.E., 1996, Modified volcanic domes and associated debris aprons on Venus, *in* McGuire, W.J., Jones, A.P., and Neuberg, J., eds., Volcano instability on the Earth and other planets: London, Geological Society Special Publication No. 110, p. 349–371.

Campbell, B.A., 1995, Use and interpretation of Magellan quantitative data in Venus mapping, 2d ed.: U.S. Geological Survey Open-File Report 95–519, 32 p.

Campbell, D.B., Stacy, N.J.S., Newman, W.I., Arvidson, R.E., Jones, E.M., Musser, G.S., Roper, A.Y. and Schaller, C., 1992, Magellan observations of extended impact crater related features on the surface of Venus: Journal of Geophysical Research, v. 97, no. E10, p. 16,249–16,277.

Chadwick, D.J., and Schaber, G.G., 1993, Impact crater outflows on Venus—Morphology and emplacement mechanisms, Journal of Geophysical Research, v. 98, no. E11, p. 20,891–20,902.

Chapman, M.G., 1999, Geologic/geomorphic map of the Galindo quadrangle (V–40), Venus: U.S. Geological Survey Geologic Investigations Series I–2613, scale 1:5,000,000.

Copp, D.L., 1997, Observations of stratigraphy and volcanism from Guinevere and Sedna Planitiae, Venus: University of London, Ph.D. dissertation, 314 p.

Copp, D.L., Guest, J.E., and Stofan, E.R., 1998, New insights into coronae formation—Mapping on Venus: Journal of Geophysical Research, v. 103, no. E8, p. 19,401–19,418.

Crumpler, L.S., Aubele, J.C., Senske, D.A., Keddie, S.T., Magee, K.P., and Head, J.W., 1997, Volcanoes and centers of volcanism on Venus, *in* Bougher, S.W., Hunten, D.M., and Phillips, R.J., eds., Venus II—Geology, geophysics, atmosphere, and solar wind environment: Tucson, University of Arizona Press, p. 697–756.

Fink, J.H., Bridges, N.T., and Grimm, R.E., 1993, Shapes of Venusian "pancake" domes imply episodic emplacement and silicic composition: Geophysical Research Letters, v. 20, p. 261–264.

Ford, J.P, Blom, R.G., Crisp, J.A., Elachi, C., Farr, T.G., Saunders, R.S., Theilig, E.E., Wall, S.D., and Yewell, S.B., 1989, Spaceborne radar observations—A guide for Magellan radar image analysis: Pasadena, Calif., Jet Propulsion Laboratory Publication 89–41, 126 p.

Ford, J.P., Plaut, J.J., Weitz, C.M., Farr, T.G., Senske, D.A., Stofan, E.R., Michaels, Gregory, and Parker, T.J., eds., 1993, Guide to Magellan image interpretation: Pasadena, Calif., Jet Propulsion Laboratory Publication 93–24, 148 p.

Ghail, R.C., 2001, The complex case of Beruth Corona [abs.], *in* Lunar and Planetary Science XXXII, abstract 1276: Houston, Lunar and Planetary Institute [CD-ROM].

Guest, J.E., Bulmer, M.H., Aubele, J.C., Beratan, K., Greeley, R., Head, J.W., Michaels, Gregory, Weitz, C.M., and Wiles, C., 1992, Small volcanic edifices and volcanism in the plains of Venus: Journal of Geophysical Research, v. 97, no. E10, p. 15,949–15,966.

Guest, J.E., Bulmer, M.H., Beratan, K., Michaels, Gregory, Desmaris, K., and Weitz, C.M., 1991, Slope failure on the margins of volcanic domes on Venus: Eos, Transactions of the American Geophysical Union, v. 72, no. 44, p. 278.

Guest, J.E., and Stofan, E.R., 1999, A new view of the stratigraphic history of Venus: Icarus, v. 139, p. 55–66.

Hamilton, V.E., and Stofan, E.R., 1996, The geomorphology and evolution of Hecate Chasma, Venus: Icarus, v. 121, p. 171–194.

Hansen, V.L., and Willis, J.J., 1996, Structural analysis of a sampling of tesserae—Implications for Venus geodynamics: Icarus, v. 123, p. 296–312.

Head, J.W., Crumpler, L.S., Aubele, J.C., Guest, J.E., and Saunders, R.S., 1992, Venus volcanism—Classification of volcanic features and structures, associations, and global distribution from Magellan data: Journal of Geophysical Research, v. 97, no. E8, p. 13,153–13,197.

Herrick, R.R., and McGovern, P.J., 2000, Kunhild and Ereshkigal, an extinct hot-spot region on Venus: Geophysical Research Letters, v. 27, p. 839–842.

Herrick, R.R., and Phillips, R.J., 1994, Implications of a global survey of venusian impact craters: Icarus, v. 111, p. 387–416.

Herrick, R.R., and Sharpton, V.L., 2000, Implications from stereo-derived topography of venusian impact craters: Journal of Geophysical Research, v. 105, no. E8, p. 20,245–20,262.

Ivanov, M.A., and Head, J.W., 1996, Tessera terrain on Venus—A survey of the global distribution, characteristics, and relation to surrounding units from Magellan data: Journal of Geophysical Research, v. 101, no. E6, p. 14,861–14,908.

Ivanov, B.A., Nemchinov, I.V., Svetsov, V.A., Provalov, A.A., Khazins, V.M., and Phillips, R.J., 1992, Impact cratering on Venus—Physical and mechanical models: Journal of Geophysical Research, v. 97, no. E10, p. 16,167–16,182.

Johnson, J.R., and Baker, V.R., 1994, Surface property variations in venusian fluidized ejecta blankets: Icarus, v. 110, p. 33–70.

Lancaster, M.G., Guest, J.E., and Roberts, K.M., 1995, Great lava flow fields on Venus: Icarus, v. 118, p. 69–86.

Lancaster, M.G., Guest, J.E., Roberts, K.M., and Head, J.W., 1992, "Great" lava fields on Venus [abs.], *in* Lunar and Planetary Science XXIII: Houston, Lunar and Planetary Institute, p. 753–754.

McGill, G.E., 1993, Wrinkle ridges, stress domains, and kinematics of Venusian plains: Geophysical Research Letters, v. 20, p. 2407–2410.

———1994, Hotspot evolution and Venusian tectonic style: Journal of Geophysical Research, v. 99, p. 23,149–23,161.

McKenzie, D.P., McKenzie, J.M., and Saunders, R.S., 1992, Dike emplacement on Venus and Earth: Journal of Geophysical Research, v. 97, p. 15,997–15,990.

McKinnon, W.B., Zahnle, K.J., Ivanov, B.A., and Melosh, H.J., 1997, Cratering on Venus—Models and observations, *in* Bougher, S.W., Hunten, D.M., and Phillips, R.J., eds., Venus II—Geology, geophysics, atmosphere, and solar wind environment: Tucson, University of Arizona Press, p. 969–1014.

Muhleman, D.O., 1964, Radar scattering from Venus and the Moon: The Astronomical Journal, v. 69, no. 1, p. 34–41.

Muller, O.H., and Pollard, D.D., 1977, The state of stress near Spanish Peaks, Colorado, determined from a dike pattern: Pure Applied Geophysics, v. 115, p. 69–86.

Odé, H., 1957, Mechanical analysis of the dike pattern of the Spanish Peaks area, Colorado: Geological Society of America Bulletin, v. 68, p. 567–576.

Pavri, Betina, Head, J.W., III, Klose, K.B., and Wilson, Lionel, 1992, Steep-sided domes on Venus—Characteristics, geologic setting, and eruption conditions from Magellan data: Journal of Geophysical Research, v. 97, no. E8, p. 13,445–13,478.

Pettengill, G.H., Ford, P.G., and Wilt, R.J., 1992, Venus surface radiothermal emission as observed by Magellan: Journal of Geophysical Research, v. 97, no. E8, p. 13,091–13,102.

Phillips R.J., Arvidson, R.E., Boyce, J.M., Campbell, D.B., Guest, J.E., Schaber, G.G., and Solderblom, L.A., 1991, Impact craters on Venus—Initial analysis from Magellan: Science, v. 252, p. 288–297.

Plaut, J.J., 1993, The non-SAR experiments, *in* Ford, J.P., Plaut, J.J., Weitz, C.M., Farr, T.G., Senske, D.A., Stofan, E.R., Michaels, Gregory, and Parker, T.J., eds., 1993, Guide to Magellan image interpretation: Pasadena, Calif., Jet Propulsion Laboratory Publication 93–24, p. 19–31.

Plescia, J.B., and Golombek, M.P., 1986, Origin of planetary wrinkle ridges based on the study of terrestrial analogs: Geological Society of America Bulletin, v. 97, p. 1289–1299.

Roberts, K.M., Guest, J.E., Head, J.W., and Lancaster, M.G., 1992, Mylitta Fluctus, Venus—Rift-related, centralized volcanism and the emplacement of large-volume flow units: Journal of Geophysical Research, v. 97, no. E10, p. 15,991–16,015.

Schaber, G.G., Strom, R.G., Moore, H.J., Soderblom, L.A., Kirk, R.L., Chadwick, D.J., Dawson, D.D., Gaddis, L.R., Boyce, J.M., and Russell, J., 1992, Geology and distribution of impact craters on Venus—What are they telling us?: Journal of Geophysical Research, v. 97, no. E8, p. 13,257–13,301.

Schubert, Gerald, Moore, W.B., and Sandwell, D.T., 1994, Gravity over coronae and chasmata on Venus: Icarus, v. 112, no. 1, p. 130–146.

Schultz, P.H., 1992, Atmospheric effects on ejecta emplacement and crater formation on Venus from Magellan: Journal of Geophysical Research, v. 97, no. E10, p. 16,183–16,248.

Shaw, H.R., and Swanson, D.A., 1970, Eruption and flow rates of flood basalts, *in* Gilmour, E.H., and Stradling, D., eds., Proceedings of the Second Columbia River Basalt Symposium: Cheney, Eastern Washington State College Press, p. 271–299.

Stofan, E.R., Anderson, S.W.. Crown, D.A., and Plaut, J.J., 2000a, Emplacement and composition of steep-sided domes on Venus: Journal of Geophysical Research, v. 105, no. E11, p. 26,757–26,772.

Stofan, E.R., Guest, J.E., and Brian, A.W., 2001a, Plains resurfacing on Venus—Examples from geographically diverse quadrangles [abs.], *in* Lunar and Planetary Science XXXII, abstract 1313: Houston, Lunar and Planetary Institute [CD-ROM].

Stofan, E.R., Guest, J.E., Brian, A.W., and Anderson, S.W., 2002, Large volcanoes on Venus—Eruptive styles and emplacement histories [abs.], *in* Lunar and Planetary Science XXXIII, abstract 1105: Houston, Lunar and Planetary Institute [CD-ROM].

Stofan, E.R., Hamilton, V.E., and Cotugno, Kristen, 1993, Parga and Hecate Chasmata, Venus—Structure, volcanism and models of formation [abs.], *in* Lunar and Planetary Science XXIV: Houston, Lunar and Planetary Institute, p. 1361–1362.

Stofan, E.R., Hamilton, V.E., Janes, D.M., and Smrekar, S.E., 1997, Coronae on Venus—Morphology and origin, *in* Bougher, S.W., Hunten, D.M., and Phillips, R.J., eds., Venus II—Geology, geophysics, atmosphere, and solar wind environment: Tucson, University of Arizona Press, p. 931–968.

Stofan, E.R., Sharpton, V.L., Schubert, Gerald, Baer, Gidon, Bindschadler, D.L., Janes, D.M., and Squyres, S.W., 1992, Global distribution and characteristics of coronae and related features on Venus—Implications for origin and relation to mantle processes: Journal of Geophysical Research, v. 97, no. E8, p. 13,347–13,378.

Stofan, E.R., Smrekar, S.E., Martin, P., 2000b, Coronae of Parga Chasma, Venus—Implications for chasma and corona evolution [abs.], *in* Lunar and Planetary Science XXXI, abstract 1578: Houston, Lunar and Planetary Institute [CD-ROM].

Stofan, E.R., Smrekar, S.E., Tapper, S.W., Guest, J.E., and Grindrod, P.M., 2001b, Preliminary analysis of an expanded corona database for Venus: Geophysical Research Letters, v. 28, no. 22, p. 4267–4270.

Strom, R.G., Schaber, G.G., and Dawson, D.D., 1994, The global resurfacing of Venus: Journal of Geophysical Research, v. 99, no. E5, p. 10,899–10,926.

Swanson, D.A., Wright, T., and Helz, R., 1975, Linear vent systems and estimated rates of magma production and eruption for the Yakima Basalt on the Columbia Plateau: American Journal of Science, v. 275, p. 877–905.

Tanaka, K.L., 1994, The Venus geologic mappers' handbook, 2d ed.: U.S. Geological Survey, Open-File Report 94–438, 68 p.

Wilhelms, D.E., 1972, Geologic mapping of the second planet: U.S. Geological Survey Interagency Report, Astrogeology 55, 36 p.

Wilhelms, D.E., 1990, Geologic mapping, *in* Greeley, Ronald, and Batson, R.M., eds., Planetary mapping: New York, Cambridge University Press, p. 208.

Zahnle, K.J., 1992, Airburst origin of dark shadows on Venus: Journal of Geophysical Research, v. 97, no. E6, p. 10,243–10,255.

Table 1. *Ancillary data for selected map units within V–39*

[The table presents information on image location, pixel scale in meters (Δ), number of pixels sampled (N), value of incidence angles (ι), and radius, together with backscatter and physical properties data: backscatter coefficient (σ_o), rms slope (θ_{rms}), Fresnel reflectivity (ρ), emissivity and calculated dielectric constants for the smooth-surface (ε_s) and rough-surface (ε_r) cases, for each sampled area. For the backscatter coefficient, values in parentheses represent the σ_o value (in dB) at plus and minus one standard deviation. All other data in parentheses represent minimum and maximum values for the selected sample area. Units that are numerous or have a large surface area were sampled more than once in widely spaced areas]

Unit label	Sample area		Pixel scale, Δ (m)	No. of pixels, *N*	Incidence angle, ι (deg)	Radius (km)
	latitude (° S.)	longitude (° E.)				
pdf	24.52187, 24.64960	221.02667, 221.13438	225	2,867	35.7	6051.971 (6051.860, 6052.049)
pdf	19.44622, 19.54197	224.49692, 224.64830	225	3,128	38.4	6051.939 (6051.887, 6052.119)
psh	0.54489, 0.89395	226.71126, 227.07559	225	28,380	45.0	6052.094 (6052.014, 6052.191)
psh	0.84500, 1.07912	225.85014, 226.16122	225	16,317	45.0	6052.263 (6052.107, 6052.407)
pu	22.99626, 23.45589	234.48390, 234.92595	225	41,664	36.4	6051.795 (6051.700, 6051.889)
pu	23.74316, 24.06235	235.44348, 235.88104	225	28,539	36.1	6051.786 (6051.666, 6051.882)
ph	7.82780, 8.07470	216.15041, 216.38481	225	12,870	43.2	6052.210 (6052.173, 6052.260)
ph	9.03249, 9.29428	216.74013, 216.95801	225	12,648	42.7	6052.188 (6051.706, 6052.482)
puT	1.12805, 1.43667	232.40642, 232.72818	225	22,192	44.9	6051.571 (6051.528, 6051.661)
puT	1.68995, 1.89428	233.39771, 233.61084	225	9,797	44.8	6051.617 (6051.543, 6051.708)
pf	8.15345, 8.48548	228.36813, 228.66945	225	22,137	43.1	6051.753 (6051.478, 6052.129)
pf	5.93183, 6.40221	227.68513, 228.15851	225	49,284	43.7	6052.538 (6052.099, 6052.743)
pli	18.89508, 19.35259	219.23604, 219.72693	225	47,304	38.6	6051.731 (6051.597, 6051.860)
pli	19.55687, 20.16971	222.97656, 223.63449	225	84,388	38.2	6051.798 (6051.622, 6051.940)
pl	2.00921, 2.19226	233.62184, 233.81584	225	8,004	44.8	6051.625 (6051.570, 6051.674)
pl	12.47563, 12.98846	235.52985, 236.01207	225	53,724	41.4	6051.934 (6051.767, 6052.084)
prT	13.58003, 13.86942	233.28308, 233.65349	225	23,290	41.0	6052.158 (6052.081, 6052.232)
prT	19.92500, 20.36761	227.88829, 228.41403	225	48,697	38.1	6052.184 (6052.098, 6052.263)
ps	23.41759, 23.79210	209.14018, 209.59059	225	34,515	36.2	6051.762 (6051.695, 6051.835)
ps	24.80714, 25.17757	221.80051, 222.26053	225	34,475	35.5	6051.713 (6051.578, 6051.910)
f	16.80705, 17.06891	231.68799, 231.93724	225	13,998	39.6	6052.213 (6052.119, 6052.331)
fN	19.42919, 19.71646	210.10640, 210.41364	225	18,632	38.3	6051.952 (6051.882, 6052.047)
fI	5.94247, 6.26812	231.11011, 231.48067	225	26,796	43.7	6051.809 (6051.060, 6051.944)
fMb	15.39815, 16.01951	215.73593, 216.03204	225	39,555	40.2	6052.642 (6052.519, 6052.729)
fL	8.85157, 9.05377	229.59763, 229.78090	225	8,256	42.8	6051.641 (6051.598, 6051.672)
fP	3.38840, 3.59273	219.55444, 219.77853	225	10,282	44.4	6052.732 (6052.554, 6052.969)
fMa	18.58653, 19.02063	224.04160, 224.52710	225	44,485	38.7	6051.764 (6051.719, 6051.820)
fG	20.84859, 21.11470	238.71954, 239.03415	225	17,514	37.6	6051.741 (6051.624, 6051.903)
fF	23.61974, 24.29642	225.80344, 226.51033	225	97,295	36.1	6051.863 (6051.724, 6052.000)
fJ	6.00632, 6.11913	214.05927, 214.14709	225	2,268	43.7	6052.269 (6052.129, 6052.380)
fV	21.65545, 21.95136	210.02344, 210.30310	225	17,220	37.1	6051.143 (6050.944, 6051.394)
vV	21.56390, 21.77040	210.42717, 210.59898	225	7,448	37.2	6051.311 (6050.837, 6051.527)
fT	12.77567, 13.16508	232.12428, 232.53717	225	34,960	41.3	6051.918 (6051.849, 6051.985)
vc	12.36498, 12.77567	233.31223, 233.75497	225	39,576	41.4	6051.731 (6051.678, 6051.785)
ef	6.26386, 6.55546	210.45833, 210.75410	225	19,182	43.6	6052.318 (6052.165, 6052.438)
vcM	7.10672, 7.22165	221.83675, 221.95697	225	3,135	43.4	6053.712 (6053.452, 6053.951)
fM_1	7.38767, 7.50473	217.90559, 218.02805	225	3,248	43.3	6052.709 (6052.676, 6052.745)
fM_2	7.24719, 7.36425	220.35498, 220.47525	225	3,192	43.3	6053.686 (6053.625, 6053.716)
fY_2	8.01510, 8.27051	213.21866, 213.51556	225	16,819	43.1	6052.346 (6052.241, 6052.477)
fY_1	11.37772, 11.53945	217.19777, 217.36945	225	6,160	41.9	6052.174 (6052.146, 6052.209)
fO	9.56455, 9.76885	211.21260, 211.44377	225	10,476	42.5	6052.513 (6052.467, 6052.541)
cO	10.88186, 11.16916	210.43956, 210.74329	225	19,176	42.1	6052.257 (6051.337, 6053.838)
fNd	20.03778, 20.28675	230.04903, 230.30302	225	13,334	38.1	6052.210 (6052.056, 6052.389)
fS	22.86645, 23.18990	228.97830, 229.35056	225	24,786	36.5	6051.688 (6051.646, 6051.723)
fOn	18.72910, 19.13767	220.26619, 220.75661	225	42,267	38.7	6051.855 (6051.771, 6051.928)
fH	11.79682, 12.22241	237.53755, 237.97937	225	41,004	41.7	6051.815 (6051.731, 6051.939)

Table 1. *Ancillary data for selected map units within V–39—continued*

Unit label	Sample area		Pixel scale, Δ (m)	No. of pixels, *N*	Incidence angle, ι (deg)	Radius (km)
	latitude (° S.)	longitude (° E.)				
fA_2	19.26109, 19.50154	237.95787, 238.19934	225	12,312	38.4	6052.271 (6052.195, 6052.365)
fA_1	18.68867, 18.88870	237.09509, 237.31100	225	9,215	38.8	6052.268 (6052.192, 6052.316)
fE_2	21.89601, 22.15999	214.02493, 214.33490	225	17,000	37.1	6051.320 (6051.233, 6051.406)
fE_1	22.13871, 22.37927	211.58372, 211.89194	225	15,390	36.9	6051.726 (6051.675, 6051.767)
fInl	20.79537, 21.29566	211.62428, 212.12564	225	52,156	37.6	6051.798 (6051.736, 6051.969)
cu_2	14.48740, 15.07045	219.97542, 220.52774	225	69,300	40.5	6051.706 (6051.578, 6051.917)
cu_1	14.77254, 15.52583	222.69260, 223.43732	225	120,345	40.4	6052.047 (6051.845, 6052.324)
fC_2	3.76300, 3.94817	214.68637, 214.92123	225	9,768	44.3	6051.784 (6051.729, 6051.841)
fC_1	4.00351, 4.62501	212.85826, 213.43063	225	78,817	44.3	6052.353 (6052.195, 6052.534)
fAt	16.58352, 16.72403	238.99922, 239.14371	225	4,422	39.7	6051.881 (6051.829, 6051.905)
fK	15.30665, 15.66840	210.43861, 210.82957	225	30,438	40.2	6052.263 (6052.194, 6052.341)
fD	7.90442, 8.39396	239.30112, 239.80873	225	54,747	43.1	6051.677 (6051.535, 6051.776)
fLe_2	0.70449, 1.03440	220.68219, 221.04657	225	26,832	45.3	6052.381 (6052.254, 6052.627)
fLe_1	0.49591, 0.15536	219.84624, 220.29152	225	33,810	45.2	6052.209 (6052.115, 6052.378)
fR_2	18.95466, 19.39089	210.65971, 211.08997	225	39,552	38.5	6051.781 (6051.520, 6051.993)
fR_1	15.10024, 15.49391	211.39587, 211.80411	225	34,596	40.3	6052.069 (6052.018, 6052.109)
cR	17.44147, 18.07588	212.84576, 213.53581	225	92,690	39.2	6052.147 (6051.760, 6052.374)
fLu	10.72864, 11.04360	234.35858, 234.66216	225	21,009	42.1	6051.129 (6050.796, 6051.662)
cLu	10.47326, 10.63926	234.08766, 234.26750	225	6,636	42.2	6051.780 (6051.660, 6051.979)
cTd	4.45261, 4.57393	211.58583, 211.66704	225	2,262	44.2	6052.051 (6051.967, 6052.195)
c	9.07505, 9.23468	229.01816, 229.16270	225	5,168	42.7	6051.808 (6051.711, 6051.971)
c	11.24790, 11.45859	218.20880, 218.51508	225	14,200	41.8	6052.133 (6051.872, 6052.557)
cf	11.04999, 11.17980	218.11728, 218.24318	225	3,658	42.0	6052.189 (6052.100, 6052.280)

Unit label	Backscatter, σ_o (dB)	Root-mean-square slope, θ_{rms} (deg)	Fresnel reflectivity, ρ	Emissivity	Dielectric constant ε_s, ε_r
pdf	–8.586 (–13.396, –6.360)	4.10 (3.60, 4.50)	0.108 (0.100, 0.115)	0.876 (0.875, 0.876)	3.2, 4.3
pdf	–8.788 (–14.695, –6.374)	2.67 (2.10, 3.40)	0.111 (0.090, 0.130)	0.879 (0.876, 0.880)	3.0, 4.1
psh	–11.190 (–14.994, –9.194)	3.36 (2.50, 4.10)	0.089 (0.075, 0.095)	0.860 (0.852, 0.867)	2.9, 4.5
psh	–12.178 (–16.272, –10.109)	3.60 (2.70, 6.10)	0.099 (0.080, 0.120)	0.862 (0.852, 0.872)	2.9, 4.4
pu	–15.602 (–17.601, –14.238)	2.16 (1.30, 3.10)	0.116 (0.100, 0.135)	0.866 (0.863, 0.869)	3.3, 4.5
pu	–13.512 (–15.430, –12.187)	1.78 (0.70, 2.30)	0.113 (0.100, 0.150)	0.863 (0.861, 0.865)	3.4, 4.6
ph	–11.012 (–13.044, –9.632)	3.36 (2.70, 3.70)	0.110 (0.100, 0.135)	0.859 (0.852, 0.864)	3.0, 4.6
ph	–10.776 (–15.010, –8.674)	3.18 (2.40, 4.30)	0.095 (0.090, 0.105)	0.872 (0.866, 0.876)	2.8, 4.2
puT	–12.656 (–14.636, –11.301)	2.38 (1.80, 3.30)	0.109 (0.080, 0.120)	0.821 (0.812, 0.829)	3.5, 5.8
puT	–13.313 (–15.723, –11.771)	3.01 (2.10, 4.20)	0.100 (0.090, 0.115)	0.828 (0.821, 0.834)	3.4, 5.5
pf	–11.709 (–18.640, –9.163)	3.52 (2.20, 4.90)	0.093 (0.075, 0.105)	0.870 (0.859, 0.876)	2.9, 4.3
pf	–10.784 (–24.172, –7.874)	3.44 (2.40, 6.30)	0.105 (0.085, 0.140)	0.868 (0.854, 0.881)	2.8, 4.3
pli	–9.984 (–19.982, –7.196)	2.67 (1.90, 3.70)	0.099 (0.075, 0.135)	0.882 (0.875, 0.888)	3.0, 4.0
pli	–13.471 (–20.412, –10.923)	2.60 (2.00, 3.20)	0.098 (0.080, 0.110)	0.882 (0.874, 0.886)	2.9, 4.0
pl	–16.346 (–18.785, –14.793)	2.26 (2.00, 2.60)	0.103 (0.095, 0.115)	0.826 (0.821, 0.829)	3.5, 5.6
pl	–15.336 (–19.896, –13.161)	2.47 (1.90, 6.20)	0.120 (0.090, 0.145)	0.841 (0.835, 0.848)	3.5, 5.2
prT	–15.491 (–18.653, –13.681)	2.26 (1.30, 2.90)	0.107 (0.090, 0.125)	0.843 (0.840, 0.847)	3.5, 5.2
prT	–15.870 (–20.458, –13.689)	2.17 (1.60, 2.70)	0.122 (0.105, 0.140)	0.871 (0.867, 0.877)	3.1, 4.3
ps	–20.290 (–24.131, –18.284)	0.75 (0.40, 1.20)	0.119 (0.085, 0.160)	0.876 (0.871, 0.878)	3.2, 4.2
ps	–17.525 (–20.345, –15.829)	1.91 (1.40, 2.80)	0.123 (0.110, 0.135)	0.848 (0.841, 0.854)	3.8, 5.1
f	–11.973 (–13.538, –8.553)	2.26 (1.60, 2.70)	0.111 (0.100, 0.120)	0.861 (0.858, 0.863)	3.2, 4.6
fN	–13.266 (–22.840, –10.503)	1.54 (1.10, 2.00)	0.098 (0.085, 0.115)	0.885 (0.880, 0.893)	2.9, 3.9
fI	–11.011 (–20.555, –8.249)	3.47 (1.50, 8.90)	0.118 (0.095, 0.175)	0.847 (0.819, 0.902)	3.2, 4.9

Table 1. *Ancillary data for selected map units within V–39—continued*

Unit label	Backscatter, σ_o (dB)	Root-mean-square slope, θ_{rms} (deg)	Fresnel reflectivity, ρ	Emissivity	Dielectric constant ε_s, ε_r
fMb	–16.711 (–22.217, –14.360)	2.55 (2.00, 3.60)	0.119 (0.090, 0.155)	0.875 (0.867, 0.890)	3.0, 4.2
fL	–10.774 (–29.084, –7.796)	3.17 (2.40, 4.80)	0.152 (0.130, 0.190)	0.850 (0.819, 0.876)	3.2, 4.9
fP	–9.163 (–10.992, –7.880)	2.03 (1.50, 2.60)	0.088 (0.080, 0.100)	0.851 (0.843, 0.857)	3.1, 4.8
fMa	–13.437 (–16.871, –11.544)	2.09 (1.50, 2.90)	0.111 (0.090, 0.140)	0.871 (0.858, 0.880)	3.1, 4.3
fG	–12.953 (–14.810, –11.657)	2.53 (1.80, 3.10)	0.089 (0.065, 0.105)	0.875 (0.867, 0.880)	3.1, 4.2
fF	–14.633 (–18.413, –12.643)	2.15 (1.40, 3.60)	0.097 (0.080, 0.115)	0.889 (0.884, 0.897)	2.9, 3.9
fJ	–10.976 (–12.575, –9.809)	5.01 (4.40, 5.80)	0.091 (0.080, 0.100)	0.901 (0.898, 0.903)	2.4, 3.4
fV	–13.601 (–18.245, –11.408)	1.60 (0.80, 3.00)	0.150 (0.105, 0.190)	0.876 (0.867, 0.886)	3.1, 4.2
vV	–8.113 (–15.340, –5.534)	2.80 (1.80, 3.50)	0.087 (0.075, 0.105)	0.892 (0.891, 0.895)	2.8, 3.8
fT	–13.076 (–19.144, –10.638)	1.80 (1.00, 2.90)	0.124 (0.105, 0.150)	0.827 (0.822, 0.835)	3.7, 5.7
vc	–15.929 (–19.065, –14.127)	2.64 (1.50, 5.60)	0.121 (0.095, 0.225)	0.835 (0.830, 0.841)	3.6, 5.4
ef	–15.293 (–18.267, –13.544)	2.36 (1.60, 3.10)	0.137 (0.120, 0.155)	0.832 (0.824, 0.840)	3.4, 5.4
vcM	–9.273 (–11.343, –7.876)	6.69 (5.30, 8.10)	0.154 (0.115, 0.220)	0.867 (0.857, 0.876)	2.9, 4.3
fM_1	–18.181 (–20.358, –16.738)	1.80 (1.70, 2.00)	0.138 (0.125, 0.160)	0.817 (0.815, 0.818)	3.7, 6.0
fM_2	–16.729 (–18.614, –15.419)	2.84 (2.50, 3.30)	0.147 (0.130, 0.185)	0.800 (0.795, 0.805)	4.1, 6.6
fY_2	–12.069 (–15.526, –10.168)	3.39 (2.70, 4.00)	0.100 (0.085, 0.115)	0.876 (0.870, 0.893)	2.8, 4.1
fY_1	–16.596 (–18.221, –15.417)	2.50 (2.20, 2.70)	0.111 (0.105, 0.120)	0.852 (0.846, 0.859)	3.2, 4.8
fO	–14.651 (–19.654, –12.388)	2.70 (2.20, 3.00)	0.096 (0.085, 0.105)	0.874 (0.865, 0.881)	2.8, 4.2
cu_2	–10.118 (–23.186, –7.216)	3.27 (2.30, 5.20)	0.096 (0.070, 0.135)	0.878 (0.870, 0.886)	2.9, 4.1
cu_1	–11.177 (–17.221, –8.744)	3.50 (2.20, 7.60)	0.091 (0.065, 0.180)	0.889 (0.869, 0.898)	2.7, 3.8
fC_2	–12.522 (–15.473, –10.781)	3.15 (2.90, 4.00)	0.103 (0.090, 0.160)	0.859 (0.852, 0.868)	3.0, 4.5
fC_1	–11.216 (–13.467, –9.741)	2.40 (1.30, 4.00)	0.077 (0.055, 0.100)	0.884 (0.869, 0.893)	2.6, 3.8
fAt	–16.830 (–18.227, –15.774)	1.85 (1.30, 2.50)	0.121 (0.110, 0.135)	0.841 (0.840, 0.845)	3.6, 5.2
fK	–18.064 (–20.459, –16.529)	1.65 (1.20, 2.10)	0.129 (0.105, 0.150)	0.852 (0.848, 0.857)	3.3, 4.9
fD	–17.946 (–19.650, –16.725)	2.48 (1.60, 3.30)	0.106 (0.095, 0.120)	0.828 (0.822, 0.832)	3.6, 5.6
fLe_2	–13.739 (–16.300, –12.138)	4.31 (3.20, 5.00)	0.103 (0.085, 0.110)	0.850 (0.843, 0.855)	3.0, 4.8
fLe_1	–15.052 (–17.407, –13.533)	2.85 (2.70, 3.70)	0.134 (0.115, 0.155)	0.796 (0.785, 0.805)	4.0, 6.7
fR_2	–12.272 (–17.863, –9.907)	2.31 (1.50, 3.90)	0.085 (0.070, 0.100)	0.897 (0.890, 0.902)	2.7, 3.6
fR_1	–15.916 (–17.719, –14.646)	2.13 (1.60, 2.70)	0.106 (0.090, 0.130)	0.867 (0.863, 0.870)	3.1, 4.4
cR	–7.581 (–17.077, –4.822)	4.05 (2.40, 7.50)	0.100 (0.060, 0.140)	0.910 (0.905, 0.919)	2.5, 3.3
fLu	–14.948 (–20.397, –12.606)	2.83 (2.50, 3.70)	0.108 (0.090, 0.145)	0.853 (0.849, 0.856)	3.2, 4.8
cLu	–9.593 (–13.686, –7.523)	3.68 (2.40, 6.30)	0.085 (0.080, 0.090)	0.861 (0.852, 0.866)	3.1, 4.6
cTd	–8.816 (–13.524, –6.610)	4.48 (4.10, 5.00)	0.091 (0.075, 0.110)	0.896 (0.894, 0.898)	2.4, 3.5
c	–8.371 (–14.527, –5.922)	3.76 (2.60, 4.90)	0.121 (0.100, 0.160)	0.870 (0.865, 0.874)	2.9, 4.3
c	–9.307 (–12.956, –6.232)	3.73 (2.10, 4.90)	0.092 (0.070, 0.115)	0.889 (0.883, 0.892)	2.6, 3.8
cf	–10.885 (–13.500, –9.265)	2.78 (2.40, 3.10)	0.092 (0.085, 0.105)	0.883 (0.878, 0.888)	2.7, 3.9
cO	–7.927 (–10.528, –6.312)	6.82 (3.70, 10.10)	0.096 (0.060, 0.170)	0.916 (0.905, 0.923)	2.3, 3.1
fNd	–15.673 (–18.131, –14.114)	1.58 (1.10, 2.30)	0.083 (0.075, 0.100)	0.880 (0.876, 0.885)	3.0, 4.1
fS	–13.235 (–15.173, –11.899)	2.67 (2.10, 3.30)	0.125 (0.110, 0.140)	0.872 (0.870, 0.876)	3.2, 4.3
fOn	–13.546 (–18.884, –11.222)	2.52 (1.50, 3.70)	0.096 (0.080, 0.110)	0.872 (0.866, 0.876)	3.1, 4.3
fH	–14.650 (–18.605, –12.615)	3.28 (2.20, 6.00)	0.107 (0.080, 0.145)	0.844 (0.832, 0.858)	3.4, 5.1
fA_2	–12.696 (–16.141, –10.799)	1.91 (1.20, 2.30)	0.120 (0.100, 0.140)	0.852 (0.847, 0.857)	3.5, 4.9
fA_1	–11.585 (–13.334, –10.341)	2.00 (1.50, 2.60)	0.106 (0.095, 0.115)	0.863 (0.859, 0.869)	3.3, 4.6
fE_2	–18.237 (–20.123, –16.927)	1.40 (1.00, 1.70)	0.124 (0.090, 0.145)	0.877 (0.871, 0.888)	3.1, 4.2
fE_1	–16.341 (–18.811, –14.777)	1.24 (0.70, 1.80)	0.119 (0.105, 0.135)	0.870 (0.867, 0.876)	3.2, 4.4
fIn	–12.749 (–18.220, –10.403)	2.07 (1.40, 2.90)	0.096 (0.075, 0.120)	0.891 (0.879, 0.897)	2.8, 3.8

Table 2. *Geologic characteristics of coronae in V–39*

[Classes (after Stofan and others, 2001b): 1, dome; 2, plateau; 3a, rimmed plateau; 3b, rim encircling raised interior; 4, rim surrounding interior below plains level; 5, rim surrounding central rise; 6, rim encircling basin with inner rim; 7, rim only; 8, basin; 9, unclassified; 10, complex. Classes 2, 5, 6, and 7 are not represented in map area]

Name	Latitude (° S.)	Longitude (° E.)	Diameter (km)	Class	Maximum altitude (m)	Base level (m)	Height above base level (m)	Geologic location
Tadaka	4	210.5	230	3b	6,052,881	6,052,476	405	Just off main rift
Fefafa	25	210.5	100	8	6,051,989	6,051,706	283	Off rift
Attabeira	1.5	211.5	240	4	6,053,529	6,052,516	1,013	Main rift
Oduduwa	11	211.5	150	3a	6,054,299	6,052,354	1,945	Veleda Linea
Inacho	20.5	212.2	125	4	6,052,192	6,051,989	203	Off rift
Among	13.2	213	210	3b	6,052,719	6,052,070	649	Off Veleda Linea
Emegelji	21.5	213.5	163	8	6,052,111	6,051,787	324	Off Jokwa Linea
Ya-Yerv	9	214	275	1	6,053,894	6,052,435	1,459	Veleda Linea
Chantico	2	215	150	1	6,055,028	6,052,597	2,431	Main rift
Pazar-ana	3	215	300	8	6,053,619	6,052,111	1,508	Main rift
Repa	13	218.8	240	7	6,052,557	6,051,746	811	Jokwa Linea
Momu	21	220.3	260	4	6,052,151	6,051,746	405	Off rift
Maram	7	221.5	600	3a	6,055,717	6,052,759	2,958	Main rift
Onenhste	19	221.5	230	4	6,052,192	6,051,908	284	Off rift
Lengdin	2.5	223	413	3a	6,053,134	6,052,011	1,123	Off rift
Ulgen-ekhe	14	224	300	8	6,052,273	6,051,949	324	Main rift
Samsing	24	229	225	8	6,052,313	6,051,706	607	Thaukhud Linea
Ndoi	20.3	230.3	225	8	6,052,557	6,051,868	689	Main rift
Blid	0.5	231.3	175	3b	6,052,273	6,051,408	865	Off rift
Beruth	19	233.5	350	3b	6,052,313	6,051,868	445	Main rift
Erkir	16.3	233.7	275	4	6,052,881	6,051,949	932	Main rift
Lumimuut	11.3	234.5	195	4	6,052,232	6,051,746	486	Just off main rift
Holla	13.2	237.7	180	9	6,052,151	6,051,746	405	Just off main rift
Aeracura	19	238.5	225	3a	6,052,557	6,051,868	689	Main rift
Rzhanitsa	17.5	214	400	10	6,052,732	6,051,948	784	Jokwa Linea
Kolias	16.5	207.9	200	1	6,053,906	6,051,700	2,206	Jokwa Linea
Dhorani	8.0	243.0	227	3a	6,052,494	6,051,354	1,140	Main rift
Atete	16	243.5	600	3a	6,053,567	6,051,824	1,743	Main rift

Table 3. *Impact craters within Taussig quadrangle*

Name	Latitude (°S.)	Longitude (°E.)	Diameter (km)
Alma	2.4	228.8	16.8
Cortese	11.4	218.4	27.7
Darline	19.3	232.6	13.0
Eileen	22.8	232.7	16.1
Felicia	19.8	226.5	11.5
Izakay	12.3	210.8	10.2
Lois	17.9	214.7	13.5
Marie	21.7	232.4	14.2
Sabira	5.8	239.9	15.7
Seiko	21.0	216.6	3.4
Taussig	9.2	229.0	25.8
von Suttner	10.6	234.9	24.0
Yenlik	16.0	225.4	8.6
Yoko	5.7	232.0	5.0